Article

Multiscale Microbial Preservation and Biogeochemical Signals in a Modern Hot-Spring Siliceous Sinter Rich in CO₂ Emissions, Krýsuvík Geothermal Field, Iceland

Jose Javier Álvaro [1,*]**, Mónica Sánchez-Román** [2]**, Klaas G.J. Nierop** [3] **and Francien Peterse** [3]

1   Instituto de Geociencias (CSIC-UCM), 28040 Madrid, Spain
2   Department of Earth Sciences, Vrije Universiteit, HV 1081 Amsterdam, The Netherlands; m.sanchezroman@vu.nl
3   Department of Earth Sciences and Geolab, Faculty of Geosciences, Utrecht University, CB 3584 Utrecht, The Netherlands; K.G.J.Nierop@uu.nl (K.G.J.N.); F.Peterse@uu.nl (F.P.)
*   Correspondence: jj.alvaro@csic.es

Abstract: The microbial communities inferred in silica sinter rocks, based on multiscale morphological features (fabrics and textures) and the presence of lipid biomarkers and their carbon isotopic composition, are evaluated in the Krýsuvík geothermal area of Iceland. Close to vent environments (T > 75 °C and pH 1.7–3), stream floors are capped with homogeneous vitreous crusts and breccia levels, with no distinct recognizable silicified microbes. About 4 m far from the vents (T 75–60 °C and pH 3–6) and beyond (T < 60 °C and pH 6–7.6), microbial sinters, including wavy and palisade laminated and bubble fabrics, differ between abandoned meanders and desiccated ponds. Fabric and texture variances are related to changes in the ratio of filament/coccoid silicified microbes and associated porosity. Coatings of epicellular silica, less than 2 μm thick, favor identification of individual microbial filaments, whereas coalescence of opal spheres into agglomerates precludes recognition of original microbial textures and silicified microbes. Episodic fluctuations in the physicochemical conditions of surface waters controlled the acidic hydrolysis of biomarkers. Wavy laminated fabrics from pond margins comprise fatty acids, mono- and dialkyl glycerol, mono- and diethers, monoalkyl glycerol esters and small traces of 10-methyl branched C₁₆ and C₁₈ fatty acids and archaeol, indicative of intergrowths of cyanobacteria, *Aquificales*, and sulfate reducing bacteria and methanogenic archaea. In contrast, wavy laminated fabrics from abandoned meanders and palisade laminated fabrics from ponds differ in their branched fatty acids and the presence vs. absence of bacteriohopanetetrol, reflecting different cyanobacterial contributions. δ¹³C values of biomarkers range from −22.7 to −32.9‰, but their values in the wavy (pond) and bubble fabrics have much wider ranges than those of the wavy (meander), palisade, and vitreous fabrics, reflecting dissolved inorganic carbon (DIC) sources and a decrease in ¹³C downstream outflow channels, with heavier values closer to vents and depleted values in ponds.

Keywords: silicified microbe; texture; fabric; biomarker; carbon isotope; microbial mat

1. Introduction

The Archean microbial record provides physical and biochemical evidence for life on early Earth, but the relationship between microbial morphological taxonomy and microbial molecular composition remains poorly constrained [1–3]. Silicified microbial communities in present-day hydrothermal systems have been studied as analogues to recognize filamentous and coccoid casts attributed to microbial life, including microbially related structures in terrestrial hot springs that date back as far as 3.5 Ga [4,5]. The discovery of surface hydrothermal silica sinters on Mars [6,7] has increased interest in sinter-related

biosignatures on Earth as a proxy to understand the origin of life itself [8,9], and the general search for evidence of life on ancient Earth and Mars [10–12]. Methods of interpreting microbial signatures in the rock record mainly rely on the recovery of biosignatures and isotopic datasets. Molecular analyses (i.e., DNA, RNA, polysaccharides, proteins and lipids) have become standard in microbial ecology, but nucleotides and proteins are relatively unstable molecules that may be rapidly degraded after the decease of the microorganisms [13]. In contrast, the occurrence and stable carbon isotopic composition ($\delta^{13}C$) of lipid biomarkers, such as *n*-alkanes, fatty acids, and *n*-alcohols, are (if well preserved) potentially geologically long-lived and can be extracted from and analyzed in the geological record [14–18].

Numerous works have highlighted the macro-, meso-, and microscopic morphological similarities between microbial mats growing in silica-saturated hot springs and ancient stromatolites [19–21]. However, a gap exists between the morphological information yielded by microbial sinters precipitated at temperatures typically lower than 65 °C, which commonly indicates that the microbial community is dominated by cyanobacterial fabrics and textures [22,23], despite the current acidic character of some sinters, and the genomical analyses from hot spring waters over 65 °C that reveal dominating archaeal and bacterial (cyanobacterial-free) communities [24]. In some areas, such as the Krýsuvík geothermal area of Iceland, the identification of thermophilic archaeal–bacterial gene sequence populations in thermal water contrasts with their scarcity or virtual absence from similar analysis made in sinter rocks from outflow channels and pond substrates. This apparent paradox is currently interpreted as the result of pH and temperature gradations, linked in the proximity of vents to extremely fast silica precipitation rates limiting (in some cases, totally preventing) microbial preservation [25,26].

In this work, we analyze microbially related structures at different scales using advanced microscopy methods, in combination with the preservation and the stable carbon composition of lipid biomarkers in silica sinters from the Krýsuvík geothermal area, one of the best studied silica-rich geothermal springs of Iceland that hosts microbial mat communities in acidic to circumneutral sinters. Geological studies of the Krýsuvík and neighboring Hengill geothermal areas have included drilling and reconstruction of magnetotelluric resistivity patterns [27], surface alteration, and associated water chemistry [28,29], monitoring of gas emissions from fumaroles, thermal water, and soil flux, and their relationship with the record of seismic activity [30–32].

rRNA sequences of water over 65 °C from the Krýsuvík geothermal area comprise about 80% of bacterial and 20% of archaeal reads, where the bacterial community is dominated by Proteobacteria and the archaeal one by Thermoproteales and Sulfolobales [24,26,33–35]. Different microbial morphotypes of silica sinters have been linked phylogenetically through cultivation-independent studies [22,25], and scanning and transmission electron microscopy identification of living cyanobacterial-dominant consortia taken from the surface of partially silicified stromatolites with a scalpel [36–39]. Specific bacterial species (e.g., *Thermus* sp. and *Rhodothermus marinus* sp.) were isolated from sinter precipitates collected in the area [40,41], whereas, despite multiple attempts, neither archaeal nor bacterial genomic sequences could be extracted [26] from a Reykjanes locality with 75 °C marine-influenced effluent.

Earlier scanning electron microscope (SEM) results from the same sinters [25] had also indicated microbial abundance was dramatically low in outflow channels, most likely due to extremely fast silica precipitation rates. Indeed, the sinter growth rates in the Krýsuvík geothermal field and the entire Reykjanes peninsula, where the geothermal waters exhibit near-neutral pH, high salinity, high temperature, and high total silica content, are among the highest in Iceland [25,38]. Thus, the Krýsuvík geothermal field represents an excellent setting for geobiological studies due to the apparent contrast between the diverse microbial community composition yielded by genomic extraction in geothermal waters and the abundance of living cyanobacteria-dominant consortia on the surface of

partially silicified stromatolites. The aims of this paper are: (i) to provide a detailed description and interpretation of differently scaled morphological features (fabrics and textures) of silica sinters, unobliterated by the development of silica crystalline forms and recorded in some stream meanders and pool floors from the Krýsuvík geothermal field; and (ii) to evaluate the microbial community composition based on morphological features and the preserved lipid biomarkers and their carbon isotopic composition.

2. Field Setting

The Krýsuvík geothermal field of SW Iceland (Figure 1a) has attracted the interest of geomicrobiological research for many decades. About 40 km^2 in extent, the geothermal field is located on the Reykjanes/Svartsengi rift segment of the Reykjanes peninsula (Figure 1b), where it is bordered by two major NE–SW-trending hyaloclastite ridges, with elevations reaching 400 m above sea level [42]. Hyaloclastites, which dominate the geological bulk in the study area, are typically formed from an assortment of pillow basalts, breccias, and tuffs. Recent resistivity measurements within the Krýsuvík system indicate a conductive body at approximately 2 to 5 km depth. The buried caldera is located near the central part of the geothermal area and coincides with the source of the inflation and deflation observed with global positioning system (GPS) and interferometric synthetic aperture radar (InSAR) measurements [27].

The Krýsuvík geothermal field contains numerous active fumaroles, extensive solfataras, hot springs, and mud pots. Six areas with active geothermal features are distinguished, and named Austurengjar, Köldunamur, Hveradalir, Sandfell, Trölladyngja, and Seltún (Figure 1c). This study is focused on Seltún (or Seltúnshverir, meaning "the hot springs at Seltún"; N63°53′49.064″ W22°3′17.117″; Figure 1d), a vapor-dominated system characterized by intensive acidic-sulfate alteration of surface rocks. Seltún comprises a stream's gradient profile of about 160 m of topographic unevenness along a distance of 800 m. The hill side shows a steep-to-slight slope gradient that influences the straight to meandering shapes of streams, which finally leave in a network of meter to decameter scale ponds next to Road 42 (Figure 1d). The flow regime is influenced by glacial melt, snowmelt, precipitation and ground water, including hot springs. Differing hydrologic energy dissipation and geochemical water conditions cause specialized microhabitats in the streams and ponds, which are colonized by variegated microbial crusts.
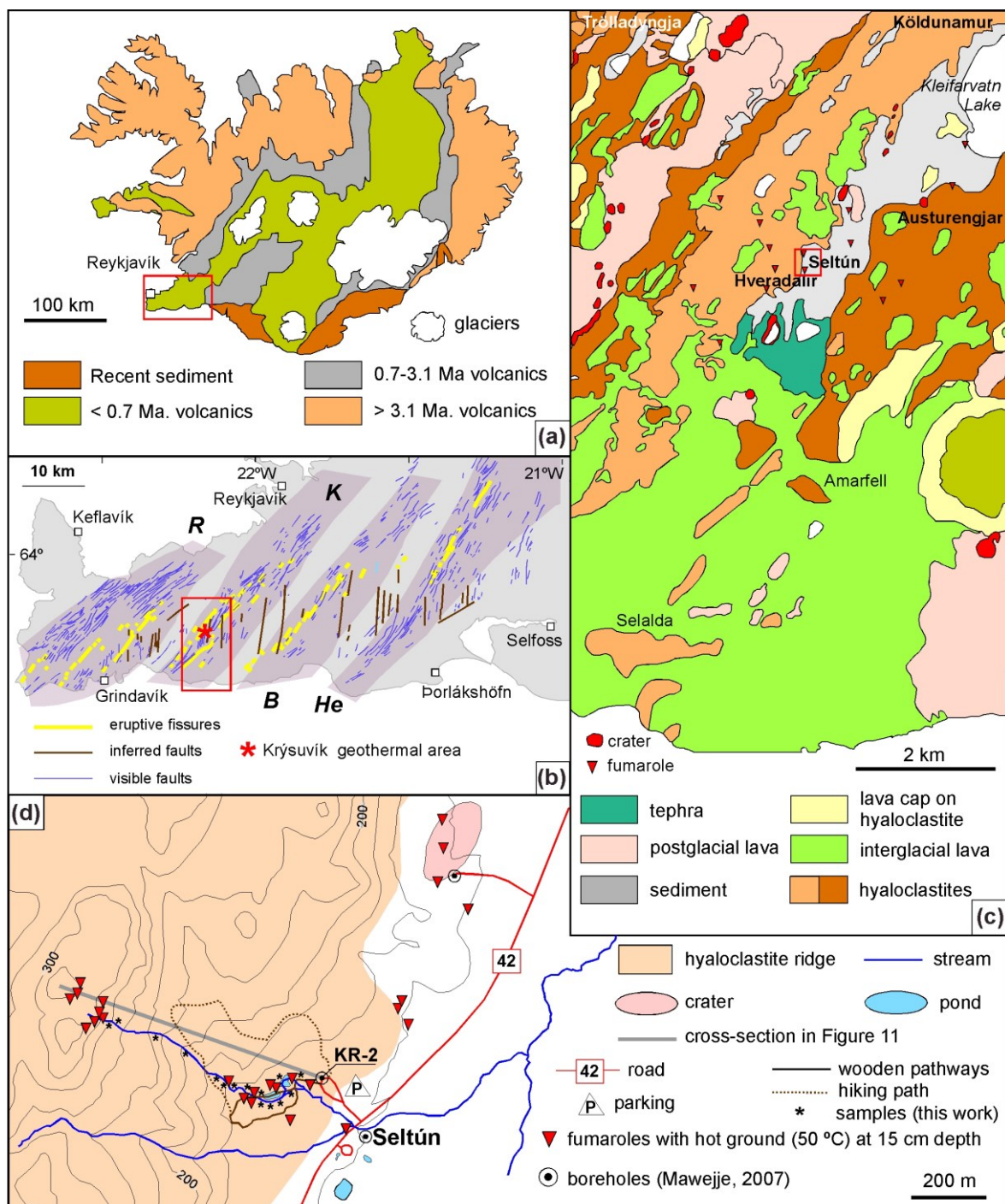
Figure 1. (**a**) Geological sketch of Iceland; based on [43]. (**b**) Setting of eruptive fissures, inferred, and visible faults throughout the Reykjanes peninsula; volcanic zones: *R* Reykjanes/Svartsengi, *K* Krýsuvík, *B* Brennisteinsfjöll, *He* Hengill; modified from [44]. (**c**) Geological map of the Krýsuvík geothermal field with location of the Seltún area; modified from [27]. (**d**) Sketch of the Seltún area showing location of streams, ponds, and sampling combined with a topographic map at scale 1:3,500.

The fumarole gases from Seltún are generally dominated by H_2O (96.9–99.4 vol%) with CO_2 as the dominant dry gas component (75.5–79.6 vol%), followed by much smaller amounts of H_2S (13.9–15.3 vol%), hydrogen (H_2: 4.8–9.32 vol%), nitrogen (N_2: 0.32–1.03 vol%), methane (CH_4: 0.02–0.08 vol%), and argon (Ar: <0.02 vol%) [31,32,45]. The geothermal spring waters are mostly acidic and locally neutral, with pH ranging between 1.7 and 7.7, caused by elevated SO_4^{2-} (10–5066 ppm) and metal concentrations, including Fe (0.05–753 ppm) and Al (0.03–390 ppm), but low Cl (1.4–17.9 ppm). The silica concentration is

variable, typically <200 ppm at <75 °C but increase with temperature and, close to boiling water, the concentration displays greater ranges (50–700 ppm) reflecting different springs sourcing silica-rich fluids [46].

The chemical composition of the ponds and related streams water at Seltún (Figure 2a–c) are characterized by intensive alteration and leaching of the volcano-sedimentary surface rock. Mineral precipitation is dominated by amorphous silica, pyrite, anatase, and kaolinite in all streams, with high-discharge areas abundant in elemental sulfur and low-discharge areas abundant in hematite and goethite [29,47]. Silica precipitation occurs both sub-aerially and sub-aqueously associated with subaerial hot springs, sublacustrine hydrothermal vents, and their discharge channels connecting them. Stream channel and pool floors are irregularly capped with colorful microbial biofilms and mats, either wholly or partly encrusted with silica. Some mats are actively fragmented by gas bubbles and spring waters, which are intermittently escaping from submerged vents. As a result, mat fragments can become buoyant, most likely due to trapped gases, and float on the water surface (Figure 2d). Their fragments are episodically blown onto the pond shorelines forming piles of mat detritus, acting as substrate for mat development along the littoral zone.
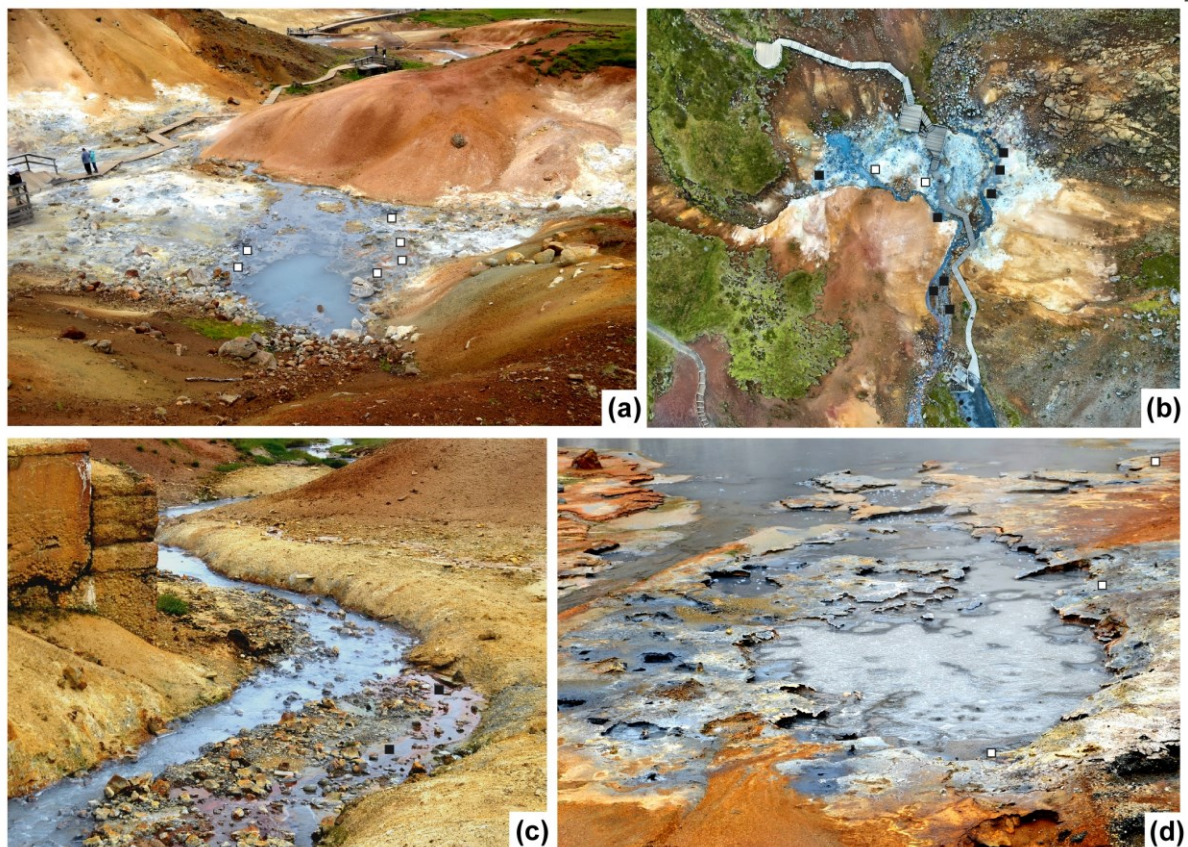

Figure 2. Field aspects of ponds and related streams at Seltún, Krýsuvík geothermal field; sampling is marked with white squares at desiccated pond margins and black squares at abandoned stream meanders. (**a**) Field view of tourist access to ponds with wooden paths (about 1.5 m wide) from the lower viewing platform. (**b**) Drone landscape photography of central pot and related streams at Seltún, fitted out with a wooden path for sightseeing tours; Alamy Stock Photo. (**c**) Lower terrace (about 1.2 m thick) crosscut by a meander; left scarp is about 1.6 m high. (**d**) Margin of mudpot showing orange- and gold-stained mats punctuated by emanating vapors; shelf is about 3 m wide.

Amorphous opal-A ($SiO_2 \cdot nH_2O$) is the dominant component of the sinter deposits in the Krýsuvík geothermal field [48], which should preclude the disappearance of textural details in microbial mats due to the transition to crystalline forms, such as opaline silica

polymorphs opal-C and opal-CT, and quartz [49–56]. However, the preservation of microorganisms is highly variable, ranging from well-preserved microbial meshwork bands to crude-laminated crusts lacking any recognizable silicified microbes.

3. Material and Methods

Sinter samples were subject to a multiscale approach (i.e., over several scales of observation) describing their fabric, textural and ultramicroscopic heterogeneities ranging from the decimeter to the nanometer scale. Depending on the chosen magnification, microscopic and geochemical data were acquired using different techniques. Fabric, textural, petrographic, and mineralogical features were used to select sinters for biomarker analysis.

3.1. Mineralogy

Forty-two sinter samples were collected from abandoned stream meanders and desiccated pond margins at Seltún (Figures 1d and 2a–d). Temperature and pH measurements of the surface water were taken along the streams at 4 m intervals, with a MW Pro + pH meter (accuracy to ±0.02 pH unit). Precipitation of silica and iron minerals and preservation of microbial cell ultrastructure were investigated by a combination of petrographic observations. Precipitation, overgrowths and cross-cutting relationships of amorphous and crystalline minerals were clarified on polished and unpolished, uncoated surfaces of sinter samples mounted on aluminum stubs via optical and FEI QUANTA 200 environmental scanning electron microscopy (ESEM). ESEM was operated under low vacuum conditions and equipped with both secondary back-scattered electron image (BSE) and energy dispersive X-ray spectroscopy (EDS) detectors. This approach allows differentiation of polyphase silica encrustation and impregnation owing to slight modifications in the geochemical composition of silica cements. SEM analyses were made in the Museo Nacional de Ciencias Naturales, Madrid, by using a JEOL JSM–6400 fitted with an Oxford Instruments D6679 detector. BSE imaging and EDS analyses were obtained by SEM with the following measurement conditions: accelerating voltage 20 kV, beam current 1–2 nÅ, and a counting interval of 50 s; analytical results display an error between ± 5% and 7%. High resolution transmission electron microscopy (HRTEM) analysis of sinter microsamples, sectioned using a diamond ultra-microtome and mounted on Formvar coated copper/chrome grids, was performed with a microscope JEOL JEM–1400 Plus from the Centro Nacional de Microscopía, Madrid, with a 120 KV accelerating voltage.

3.2. Lipid Biomarkers

Selected sinters were air dried, wrapped in aluminum foil, and then placed into plastic bags for transport to the laboratory and storage prior to analysis. Samples were subsequently treated with maximum precautions to avoid contamination introduced during residence or laboratory workup process: all samples were separated into interiors and exteriors, and analyzed in parallel with procedural blanks. Sample/procedural blank ratios were calculated for relevant analytes and, where exceptionally lean samples were deemed to have contaminated in the laboratory, these were excluded from consideration. As previously detailed [57,58], the distribution of hydrocarbons and (if present) plastic-derived contaminants can frequently reveal if samples are partially (i.e., externally) or pervasively contaminated. Such comparisons showed no significant differences for most samples that were used in this study. Some samples contained typical animal-derived biomarkers (e.g., cholesterol), suggesting a secondary overprint of the expected microbial biomarker signal. Even though these samples did not display apparent human-induced contamination, as described above, and would have fitted the general biomarker patterns, these samples were also excluded from consideration.

Ground and homogenized silica sinters (1–50 g) were ultrasonically extracted using either a mixture of dichloromethane-methanol 2:1 (v:v) for 5 times at 10 min (samples of

which only 1 g was available), or Soxhlet with a mixture of dichloromethane-methanol 7.5:1 (v:v) for 24 h (remaining samples). The obtained total lipid extracts (TLEs) were dried over Na_2SO_4 followed by evaporation of the solvent by a gentle stream of N_2. Elemental sulfur, ubiquitous in all samples, was removed from the TLEs by activated copper nodules overnight. Prior to analysis, the TLEs were silylated using *bis*(trimethylsilyl)trifluoroacetamide (BSTFA) in pyridine at 60 °C for 20 min to convert hydroxy and carboxylic acid groups into the corresponding trimethylsilyl (TMS) ethers and esters, respectively.

TLEs were dissolved in ethyl acetate at concentration of 2 mg/mL and on-column injected on a Hewlett Packard gas chromatograph (GC) with a flame ionization detector (FID) and either on a Thermo Trace GC Ultra Trace DSQ (Thermo Fisher Scientific, Waltham, MA, USA) or on an Agilent 7890B GC-5977B MSD (Agilent Technologies, Santa Clara, CA, USA) gas chromatograph–mass spectrometer (GC–MS) onto a CP-sil 5CB fused silica column (30 m × 0.32 mm i.d., film thickness 0.10 μm). The GC–FID was operated at constant pressure of 100 kPa, whereas both GC–MS instruments were operated at constant flow of 1.0 mL/min. The oven of each GC was programmed starting at 70 °C to rise to 130 °C at a rate of 20 °C·min^{-1} and then to 320 °C at a rate of 4 °C·min^{-1}, followed by an isothermal hold for 20 min. The MS operated within a scanning range of *m/z* 50–800. Major compounds were semi-quantified by integrating its peak area in the chromatogram. Relative proportions of each compound in a given sample were calculated as % of the total quantified peak area (sum of all products set at 100%). For this purpose, an internal standard (squalane) was co-injected onto the capillary column.

Compound specific $\delta^{13}C$ values were determined using GC-isotope ratio-mass spectrometry (GC–IRMS) with a Thermo Finnigan Delta-Plus XP mass spectrometer. A similar column, gas flow and oven temperature program were used as described above for the GC–MS. Carbon isotopic compositions are reported relative to the Vienna Pee Dee Belemnite (VPDB) standard and are based on duplicate analyses of well-resolved peaks. The $\delta^{13}C$ values for the alcohols and fatty acids (FAs) were corrected for the isotopic composition of carbon added during derivatization. The $\delta^{13}C$ value of the BSTFA, or in fact the TMS group added, used for silylation was determined by derivatization of *myo*-inositol with a known $\delta^{13}C$ composition.

4. Multiscale Structures of Sinter Samples

This section comprises the description and interpretation of microbially related sinter structures sampled at Seltún. Samples are analyzed at three scales, which include the mesoscale (1–100 mm), the microscale (10–1000 μm), and the individualized silicified microbes (<10 μm). Determination of the organic matter/silica ratio is made at the scale of textural inter-laminae.

4.1. Sinter Fabrics (Mesoscale 1–100 mm)

The term fabric refers here to the arrangement of elements (including mineral type, organization of opal clusters, and microbial laminae and textures) that makes up the sinter samples. The fabric can be studied in outcrop, hand specimen and under microscope. We include here the "matrix fabric types", "lithofacies", "biofacies", "biofabrics" and "microfacies" concepts previously reported in the literature [50,51,59–65].

Stream meanders show three characteristic fabrics dominated by wavy laminated and bubble sinters, locally interrupted by homogeneous vitreous crusts (Figure 3a,b) in the surroundings of vents. Desiccated pond margins also include wavy laminated, bubble and palisade laminated fabrics (Figure 3c,d). The three fabrics are episodically interrupted by scouring breccia and sandy deposits (Figure 3e).

(i) Wavy laminated fabrics [66] were sampled on stream meanders and ponds (T < 65 °C and pH > 3). They are composed of subparallel crinkled-to-undulating laminae, up to 4 cm thick and exhibiting distinct light/dark grey alternations. Laminae show upward gradual modifications from tabular to domal and subsidiary pseudo-columnar geometries, up to 1 cm in diameter, with equidimensional to asymmetric structures (Figure 3a,b).

Total fenestral porosity is less than 10% in volume. Fenestral types are dominantly laminoid and ovoidal in shape, up to 1 mm thick; in domal shapes, ovoidal pores become vertically and radially elongated. The fabric exhibits sharp contacts with the palisade laminated and bubble fabrics described below. The laminae of the overlying bubble fabric adapt its shape to the irregular outline of the fenestral pores that mark the fabric contact. The laminae can also be locally broken and disconnected laterally by low-angle scoured surfaces (see arrows in Figure 3a), which represent erosive contacts with overlying breccia levels.

(ii) Bubble fabrics [19,63] were sampled on stream meanders and ponds ($T < 65$ °C and pH > 3). These "bubble-associated fenestrae" [67] or "bubble mat textures" [68] form friable, highly porous sinter rocks, locally marked by the presence (or even absence) of a crude laminated, fenestral silica (Figure 3b). The presence and arrangement of millimeter- to centimeter-sized fenestrae affect both porosity and permeability. Larger pores display laminoid and subelliptical-to-subcircular outlines, parallel to bedding. Where the bubbles become flattened and elongated, the overlying silica laminae become wavy. Thus, the morphology of the laminae overlying the bubble fabric is highly controlled by the irregular substrate shape of bubble sinters. Bubbles are commonly formed due to trapped gas bubbles under the mat surface or decayed microbial mats in the sediment [50,69]. Gas bubbles are commonly trapped within the microbial exopolymeric substances (EPS) matrix, producing voids; the roundness of their voids is controlled by the flow rate of spring discharges [68].

(iii) Palisade laminated fabrics are conspicuous in ponds ($T < 40$ °C and pH 6–7.6). These mats show micro-pillar to dendritic shrub-like masses showing upward branching growth patterns (Figure 3c,d) that are usually bound by upper and lower laminae [70]. Individual dendrites are typically densely microbial masses, up to 4 mm high, with distinct highly irregular margins. They show distal elongation and expansion, and commonly develop broad inflated branches that produce shrub-like masses ranging from compact and squat, to elongate and dendritic in shape [52,66,71]. As a result of the micro-pillar arrangement, the porosity is regularly spaced and elongated, and oriented primarily surface-perpendicular [72]. The resulting laminae consist of dendritic sublaminae alternating with smooth vitreous crusts and wavy laminated fabrics.

(iv) Homogeneous vitreous crusts form coatings of straight and meandering streams interrupted by vents ($T > 75$ °C and pH < 3). They form dense and massive laminae, up to 4 cm thick with porosities less than 5% in volume. The crusts, whitish to vitreous in color, grade both vertically and laterally to the wavy laminated and bubble fabrics. A crude lamination is locally observed.

(v) The stream-bed fabric [64] is mainly associated with the homogeneous vitreous crusts. It consists of interbedded clast- and matrix-supported conglomerates, litharenites, and breccia levels. These deposits, brownish in color, contain angular to subrounded basaltic clasts, rich in partly weathered olivine and pyroxene grains (with irregular margins and alteration rinds), and reworked pumice clasts, as well as clasts derived from the microbial fabrics described above (Figure 3e), set in a coarse sand-to-granule matrix. The basal contact of the fabric is scouring and its top gradual. Both low-angle and parallel lamination and normal and inverse grading are observed.
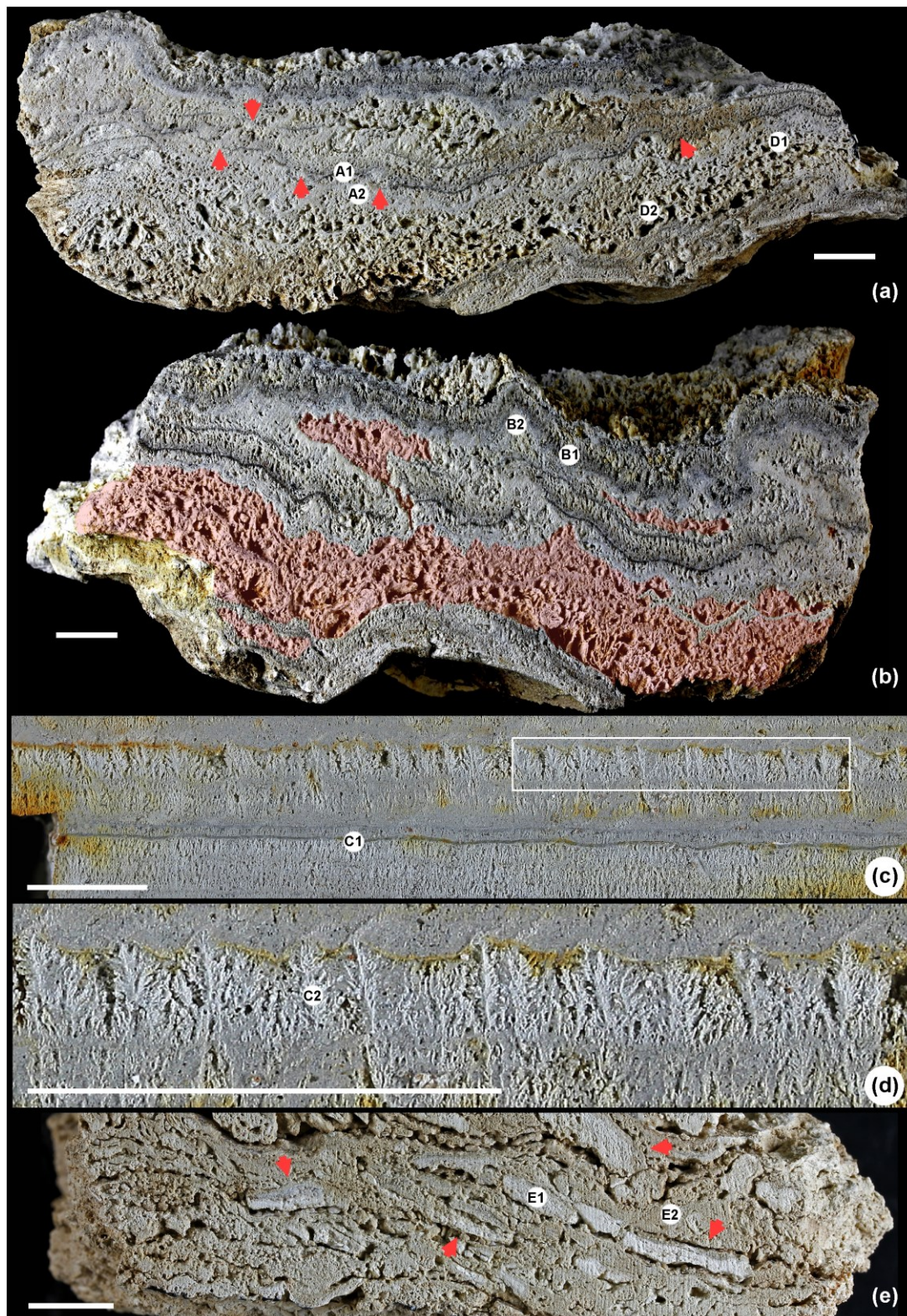
Figure 3. Polished sinter slabs from Seltún. (**a**) Wavy laminae (about 1 mm thick) adapting to geometry of bubble sinters (dyed red in Figure 3b) from a pool margin; well-indurated silica shows light-to-dark grey gradations (textures) and scouring contacts (red arrows) interrupting laminae; scale bar = 1 cm. (**b**) Alternating wavy laminated (with alternating light to dark grey textures) and bubble fabrics from an abandoned meander channel; scale bar = 1 cm. (**c**) Alternations of stacked palisade laminae (<1 cm thick) and well-indurated silica; scale bar = 0.5 cm. (**d**) Detail of previous image (boxed area) showing branching geometries; scale bar = 0.5 cm. (**e**) Breccia deposit of silica clasts embedded in silica crust indicating reworking of vitreous fabric sinter rocks; scale bar = 1 cm. Abbreviations: A1, A2, B1, B2, C1, C2, D1, D2, E1, and E2 mark provenance of biomarker samples.

4.2. Sinter Textures (Microscale 10–1000 µm)

The term texture refers here to smaller-scale features of the rock, generally described using a microscope, and including microbial/grain size and shape and inter-microbial/granular relations. Wavy laminated, bubble and palisade laminated fabrics share common textures that grade both vertically and laterally. Their relative abundance controls the fabric (mesoscopic) appearance. When observed under the microscope, the laminae show a finer-scale sublamination that is not readily observed in hand specimen. Three distinct styles of sub-millimetric lamination are observed:

(i) Some light/dark alternations of the wavy laminated fabric can be subdivided into sublaminated packages separated by truncated surfaces (Figure 4a), which reflect interruption of microbial growth by scouring and, in some cases, clastic sediment deposition. Each package, up to 2 mm thick, does not show subparallel, but highly-porous meshworks of convex-up sublaminae, which display upward decreases in porosity and pore shape grading from laminoid to ellipsoidal outlines. In 2D thin-sections, microbial packages exhibit onlapping features related to the episodic character of microbial growth. Under ESEM, the sublaminae show sparsely packed meshworks of filamentous microbes and subsidiary coccoids, which form highly porous textures or crudely lie parallel to the growth surface (Figure 5a).

(ii) Other light/dark alternations of the wavy laminated fabric consist of subparallel wrinkled, wavy, and smooth sublaminae that form biofilms with variable patterns of fenestral porosity. Flat sublaminae grade upward into domal and, locally, pseudo-columnar shapes (Figure 4c,d). Non-branching columns show vertically equal widths and upward thinning pencil shapes. Pseudo-columnar stromatolites display uniform inclinations up to 30° from the vertical. They show partly laterally linked laminae, transitional to laterally linked (LLH), pseudo-columnar stromatolites. A decreasing degree of lateral linkage is conspicuously accompanied by increasing influx of sediment. Neighboring columns are separated by gaps, up to 2 mm wide, which decrease in width upward as the columns grew; the gaps are open or partly occluded with oncoids (Figure 4f), detrital grains, and/or pore-filling silica. This texture reflects varying sediment trapping and binding activities with alternating modes of flat, domal, and columnar growth suggesting episodic changes in hydrodynamic conditions. The action of bottom currents may also be interpreted by the uniform inclination of columns and by their elongated basal cross-sections.

Under ESEM, the lighter sublaminae consist of densely interwoven, flat-lying filaments (Figure 5b) displaying low porosities. The lighter sublaminae alternate with darker sublaminae and, when pores increase in size and density, become bubble sinters. The darker layers are composed of densely packed rod-shaped and coccoid-dominated clusters and isolated opal-A spheres, with subsidiary filaments, arranged subparallel to the sublaminae (Figure 5c). Where these clusters misplace their subparallel arrangement, they form highly-porous (bubble-style), filament-coccoid meshworks.

(iii) Both kinds of light/dark alternations of the wavy laminated fabric can be sharply overlain by palisade laminations (Figure 4b,g–h). These are formed by a superposition of sublaminae, up to 500 µm thick, dominated by erect filaments aligned parallel to each other and subtransverse to the growth surface. Branching, if present, may be diverging dendroid or parallel and branches are usually <1 cm long and densely growing. The orientation of the long axes is not strictly parallel to each other, probably reflecting the influence of weak currents. Under ESEM, the preserved cells form loosely interwoven, branching and non-branching filament bundles separated but vertically oriented pores (Figure 5d).

(iv) The gradual impoverishment in microbial remains leads to the occurrence of vitreous crusts. They display agglomerates of abiotic opal-A spheroids, which will described in detail below (Figure 5e).
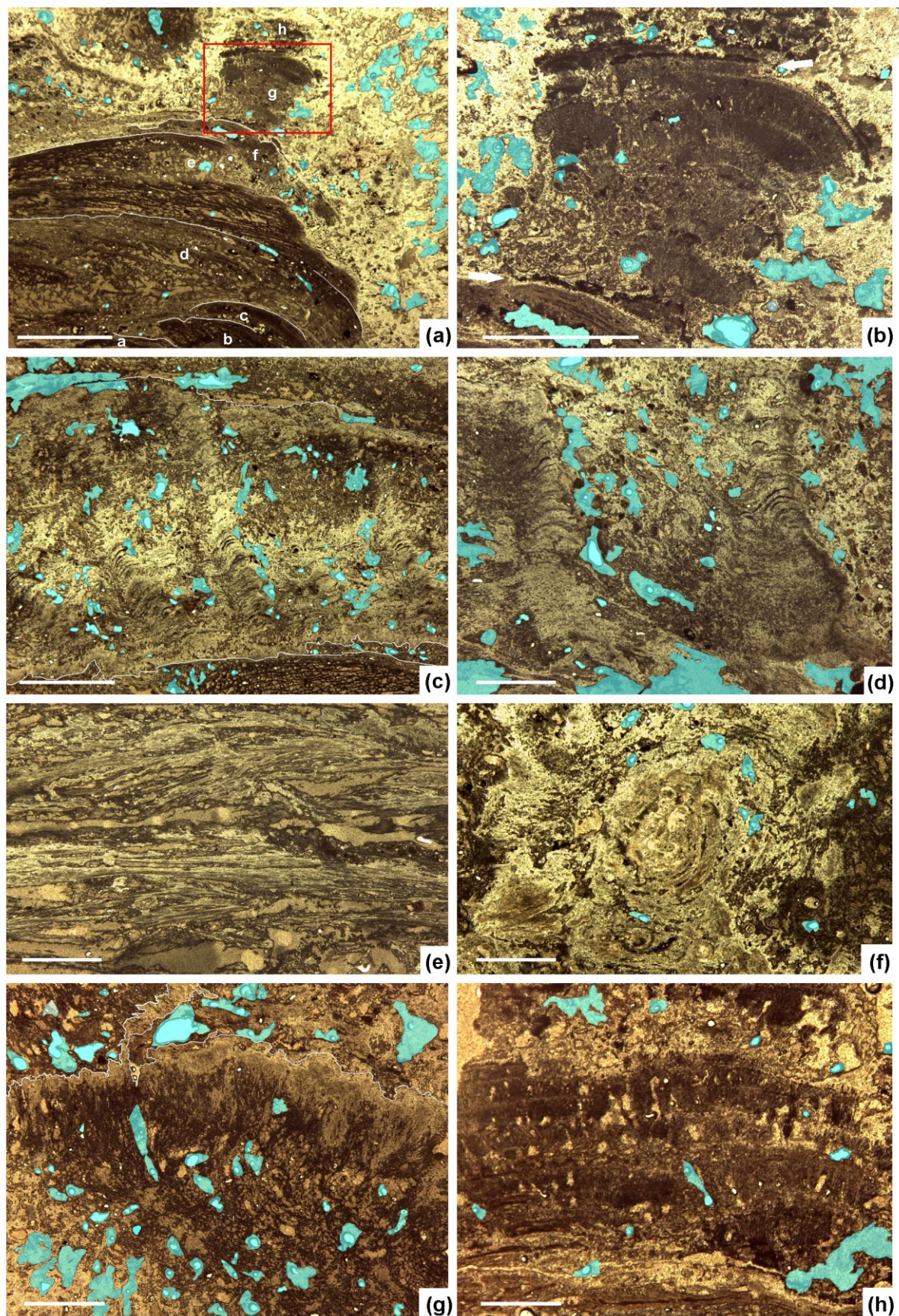
Figure 4. Representative optical photomicrographs from the petrographic study of the Seltún sinter exhibiting two-dimensional (2D) textures in transmitted plane light. (**a**) Superposition of microbial packages (*a* to *h*) showing onlapping features;

lower packages show repeated upward decreases in laminoid-to-subelliptical porosity; microbial lamination are not sub-parallel, but display a superposition of convex-up sublaminae. (**b**) Detail of boxed area in previous picture (package labelled *g*), with palisade laminated fabric bounded by sharp (arrowed) contacts. (**c,d**) Pseudo-columnar (pencil-like) micro-stromatolitic laminae up to 5 mm high and 1.8 mm in basal diameter. (**e**) Microbial laminae adapting to laminoid pores and exhibiting crinkled features. (**f**) Microbial oncoid up to 2 mm across. (**g**) Bunch of microbial laminae subtransverse to stratification. (**h**) Superposition of palisade laminae, each one up to 400 μm thick; larger pores artificially stained in blue; scale bars = 2 mm (for Figure 4a,c) and 1 mm (for Figure 4b,d–g).
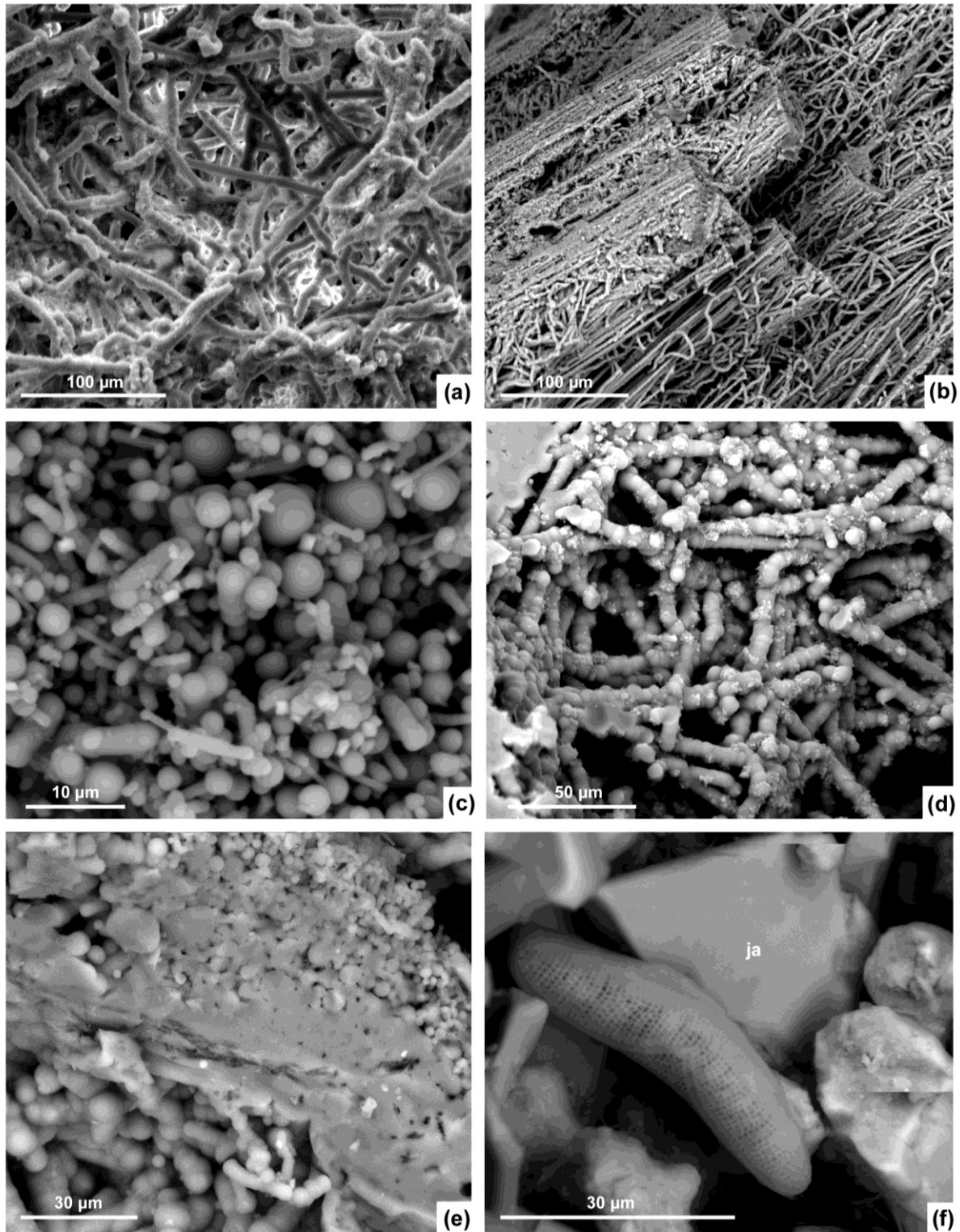
Figure 5. Environmental scanning electron microscopy (ESEM) images of Seltún sinter exhibiting 3D textures. (**a**) Sparsely packed meshwork of chaotically arranged microbial filaments forming highly porous growth frameworks. (**b**) Densely interwoven, flat-lying filaments, forming packets about 50 μm thick. (**c**) Clusters of densely packed rod-shaped and coccoids forming porous growth frameworks. (**d**) Loose interwoven filament bundles. (**e**) Silica crust showing agglomeration of opal spheres. (**f**) Diatom embedded in a microbial network including jarosite rhombohedral crystals (ja).

Under the millimetric scale, what was named fenestral porosity in the fabric description (Figure 4e) becomes a microbial "growth framework" controlled by the arrangement of individual microbes (Figure 6a). In some cases, pores are arranged in an alveolar framework of dense arrays of entangled filaments forming subparallel to low-angle sublaminae (Figure 6b), mimicking characteristic "hourglass structures" [19] (Figure 6c). Some subhorizontally arranged pores are vertically connected by sharp shift-like and zig-zag pores (Figure 6d), probably related to the upward migration of gas bubbles through partly indurated inter-laminae. All of these pores can remain open, be partly occluded with opal-A agglomerates or exhibit geopetal sediment floors composed of silica and zeolite/clay mixtures (Figure 6e). Finally, the siliceous microbial laminae become, in some samples, diatomaceous mats and stromatolites due to the conspicuous occurrence of diatom frustules (Figure 5f).
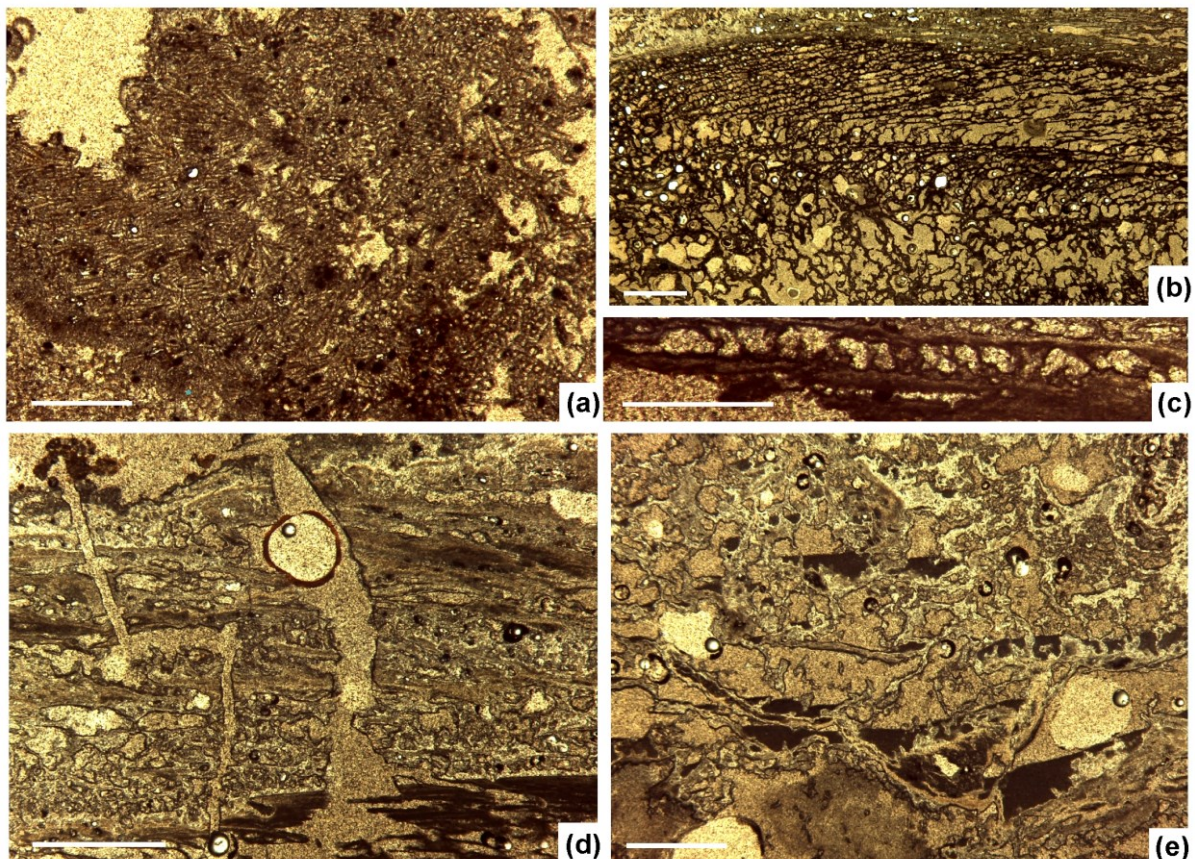
Figure 6. Thin-section photomicrographs of Seltún sinter exhibiting 2D porosities in transmitted plane light. (**a**) Meshwork of chaotically arranged microbial filaments encased in a primary fenestral pore. (**b**) Upward modification of ellipsoidal-to-laminoid fenestral pores in the onlapping microbial packages shown in Figure 6a. (**c**) Detail of fenestral pores separating two microbial laminae mimicking hourglass structures [19]. (**d**) Network of vertical pores (up to 500 μm in size) connecting fenestral (laminoid-dominant) pores, probably reflecting upward escape of gas bubbles in a partly indurated sediment. (**e**) Laminoid fenestral pores showing geopetal sediment floors composed of zeolite/clay mixtures; scale bars = 2 mm (for Figure 6a,e) and 1 mm (for Figure 6b–d).

The relative carbon content of the light/dark grey alternations from the wavy laminated and palisade fabrics were compared in sinter samples under EDS and BSE-ESEM

analyses. The C:Si (atomic/molar percentage) ratio, an interpolation of the degree of silic-ification of microbial matter, was semi-quantitatively analyzed. EDS and BSE-SEM obser-vations on the organic-rich remains, coupled with X-ray measurements (pin-point chem-ical analyses and elemental mapping) confirmed an inverse relationship between organic matter content (element C) and partial silicification (element Si; Figure 7). The C:Si ratio ranges from ~1:6 in the white microbial laminae of the wavy laminated and palisade fab-rics to ~1:3 in the dark grey microbial laminae, reflecting distinct alternations in the con-tent of organic matter in the wavy and palisade laminae.
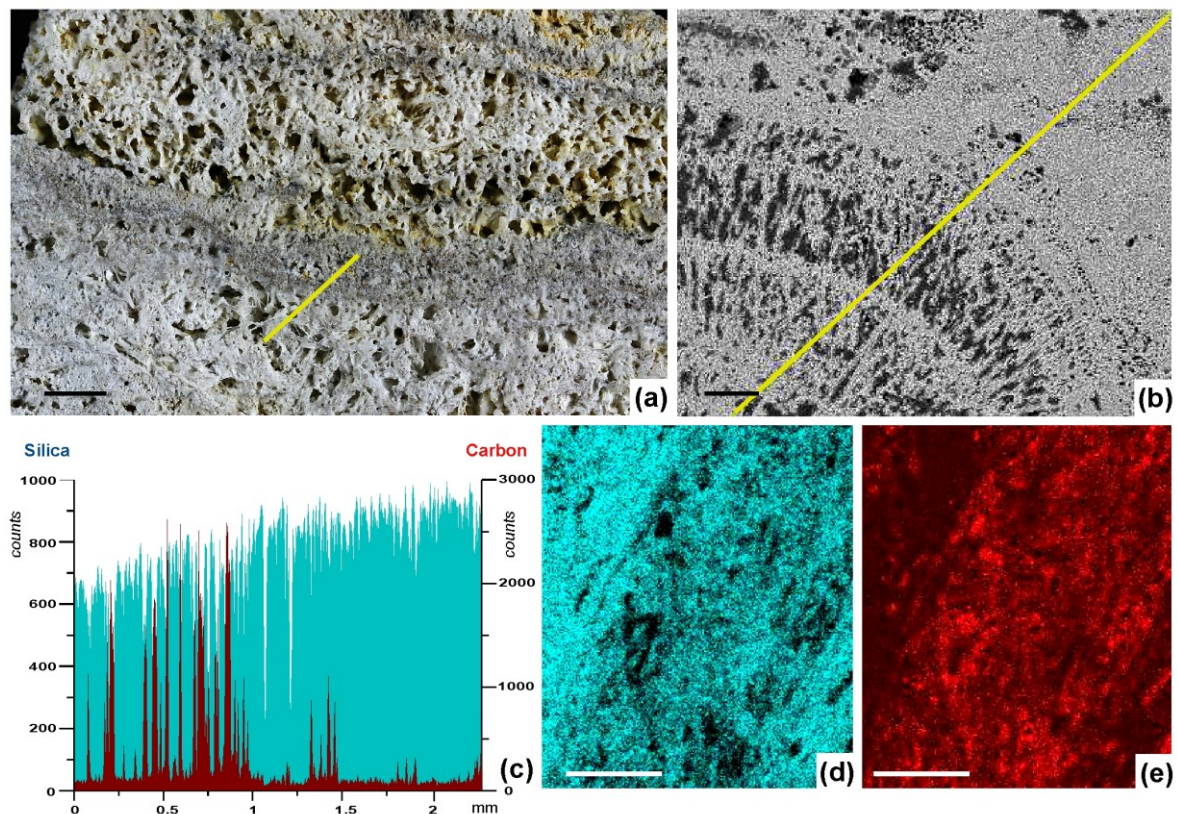

Figure 7. Modifications in the organic matter/silica ratio based on EDS and back-scattered electron image (BSE)–ESEM analyses. (**a**) Uncoated slab of laminated sample exhibiting distinct alternations of (highly porous) yellowish white and grey laminae. (**b**) Backscatter ESEM micrograph (from boxed area in previous picture) showing cross-section (yellow line) analyzed in following pictures. (**c**) Energy dispersive X-ray spectroscopy (EDS) line profiles of silica (blue) and carbon (red) showing sharp modifications in the C/Si (atomic/molar percentage) ratio, ranging from ~ 1/6 in the white to ~ 1/3 in the dark grey alternations. (**d,e**) EDS color-coded elemental maps of silica (blue) and carbon (red); elements below 5 wt% appear blurry; scale bars = 3 mm (for Figure 7a) and 1 mm (for Figure 7b,d,e).

4.3. Silicified Microbes (scale < 10 μm)

The entangled textures described above are composite frameworks formed by aggre-gations of distinct silicified microbes, recognizable by their casts. Dominant morphs are:

(i) Densely to loosely interwoven, branching and unbranching, empty filamentous microbes. These are isodiametric, up to 5–7 μm wide, 100 μm long, and with walls up to 0.5 μm thick (Figure 6a,b). They can be straight, twisted or spirally coiled chains of cells. Filaments are commonly septate or interrupted by constrictions, separating intra-filamen-tous cells that can become barrel-shaped segments, 0.8–1.5 μm thick (Figure 6d, Figure 8a–i). Lumen is 0.5–1.0 μm across. Filamentous ends can be pointed to subrounded. Silic-ified trichomes are not observed. The outer wall surface ranges from smooth to rough and irregularly mammillated. Filaments can be preserved attached vertically or horizontally

to the substrate. Some silicified filaments exhibit distinct changes in diameter, morphology and surface texture of the opaline spheroids from the silicified inner wall to the outermost zone of encrusting precipitates.

Filamentous microbes are dominant in the light laminae that form the dark/light couplets of the wavy laminated, bubble and palisade laminated fabrics. The shape, size, and septate character of the filaments reflect cyanobacterial features. Within the Cyanobacteria, some thermophilic filamentous phototrophs retrieved from terrestrial thermal systems belong, among others, to the genera *Anabaena*, *Calothrix*, *Fischerella*, *Oscillatoria*, *Phormidium,* and *Spirulina* (for a summary of their morphological features, see Table 1). In the absence of RNA sequence analysis and trichome preservation, these filaments are considered here as morphotypes (or morph species) that co-occur in meshworks and even reflect some kind of morphological plasticity (see Figure 8a–i). Thermophilic cyanobacteria and other phototrophic prokaryotes do not occur in hydrothermal waters below pH 4, and only a few species occur below pH 5 [73].
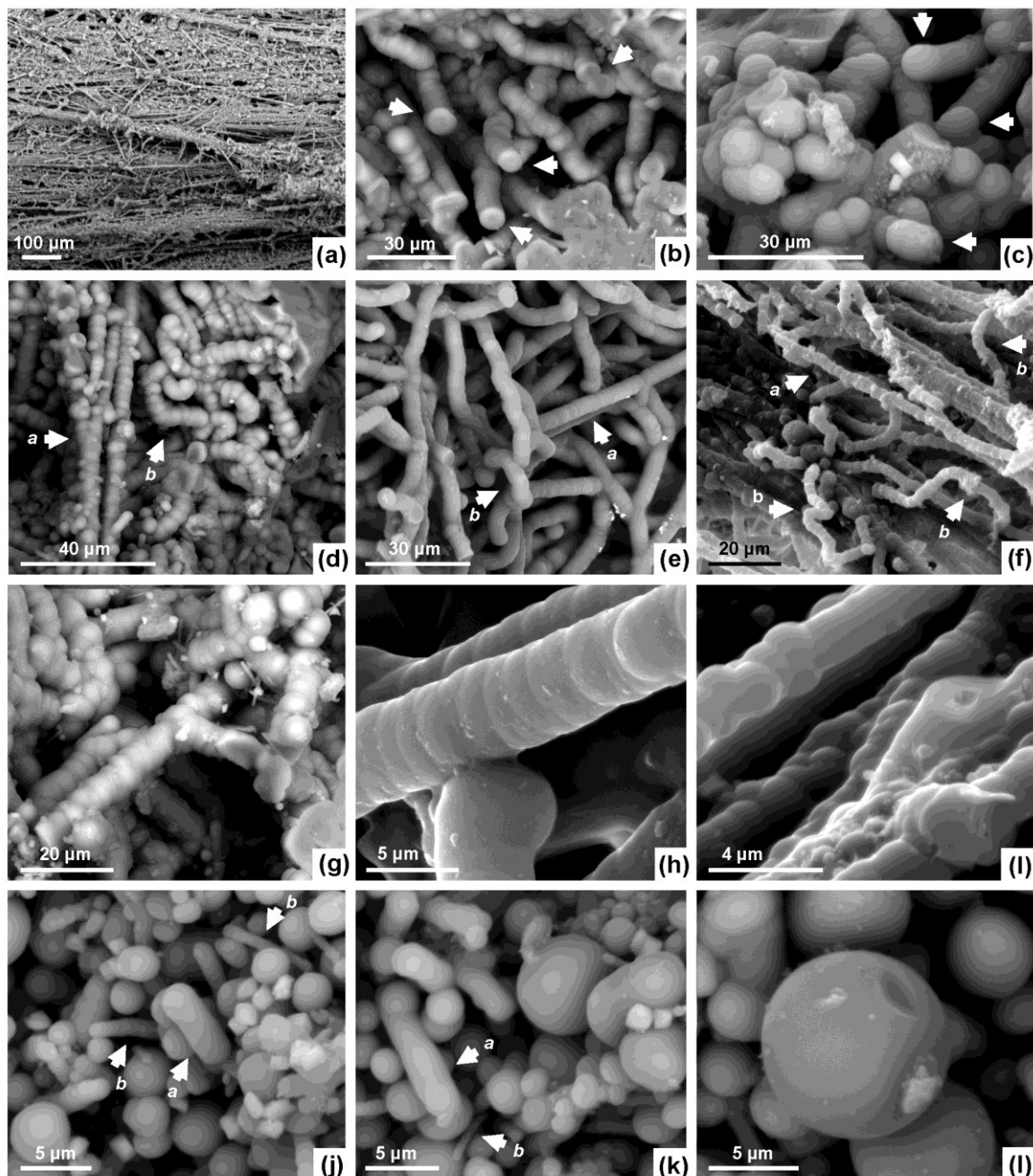
Figure 8. ESEM images of silicified microbes from the Seltún sinter. (**a**) Straight filaments with bimodal diameter sizes (peaks at 5 and 20 μm) forming a wavy laminated fabric. (**b**) Coiled and contorted filaments with arrowed flat ends (*Calothrix* morph). (**c**) Coiled and contorted filaments with arrowed thicker cap ends (*Phormidium* morph). (**d–f**) Microbial meshworks of septate filaments with straight and bifurcating (*a*) vs twisted and spiral (*b*) shapes. (**g**) Filamentous-forming T-shaped branching filaments. (**h**) Superposed filaments mimicking branching. (**i**) Cross-section of a filament showing central lumen. (**j**,**k**) Clusters of filamentous, barrel-shaped to short filaments (*Fischerella* morphs) with bimodal length/diameter ratio distribution (peaks at 3:1 and 8.5–9:1) mixed with opal-A spheres and jarosite crystals; barrel-sh. (**l**) Single opal-A sphere with lateral indentation reflecting the setting of an inner hole.

Table 1. Summarized morphological features and ecological (temperature and pH) conditions of cyanobacteria, other bacteria and red algae living in hot spots of Iceland and Yellowstone National Park and microbial cultures of their communities controlled under laboratory conditions; L length, Ø diameter; summary after [38,69,74–87]; * cyanobacteria isolated from the Krýsuvík geothermal field after [38,88].

		Temperature Range (°C)	pH Range	Morphology and Size
Bacteria				
Aquificales	*Aquifex*	85–95	6.8–9.0	rods, L 2–6 μm, Ø ~ 0.5 μm
	Sulfurihydrogenibium	79–83	<8.8	rods, L 0.5–2.8 μm, Ø 0.5–1.0 μm
	Thermocrinis (*ruber*)	82–88	7–10	rods (L < 5 μm) to filaments (L > 30 μm long, Ø ~ 0.5 μm)
FeOB	*Acidithiobacillus*	25–30	<4.0	rods, L < 3 μm, Ø ~ 1 μm
	Gallionella	<47	7.0–7.4	helical filaments
	Leptothrix	35–37	7.0–7.4	sheathed filaments, L < 20 μm, Ø ~ 1 μm
Cyanobacteria				
	Anabaena	<30	7–10.5	sheathed filamentous trichomes with constrictions at cross-walls, L < 20 μm
	Calothrix	<40	7–10	sheathed filamentous trichomes, potential branching, L < 3 mm, Ø 15 μm
	Chloroflexus	55–70	7.5–7.7	unbranched sheathed filamentous cells (trichome), L 4–7 μm, Ø 0.6 μm
	Fischerella	28–64	6.8–9	barrel-shaped to short filamentous trichomes, potential branching, L < 10 μm, Ø 5 μm
	Oscillatoria	20–30	7–7.5	unbranched filaments with straight trichome
	Phormidium	60–65	8.5–8.7	unbranched, septate filaments with calyptra (thicker cap) at edge, L < 3 μm, Ø 1.5–3 μm, lumen Ø < 1 μm
	Spirulina	30–35	7–10	coiled filamentous trichomes, L 50–300 μm, Ø 10 μm
	Synechococcus (*vulcanus*)	50–70	>6.5	subspherical, Ø < 6 μm
Eukaryotic red algae (Cyanidiales)				
	Cyanidium	35–55	0.5–5	subspherical, Ø < 10 μm
	Galderia	35–55	0.5–5	subspherical, Ø < 10 μm
	Cyanidioschyzon	35–55	0.5–5	subspherical, Ø 1–2 μm

(ii) Globular to semi-spherical clusters comprise agglomerates of rod-shaped (bacilli) and coccoid bacteriomorphs, with a small central opening (about 0.5 μm in diameter) and with thin (<0.1 μm) multi-layered walls. Rods are 8–10 μm long and about 1.4–3 μm in diameter (Figures 5c and 8j,k), whereas subspheres display a polymodal distribution with diameters up to 6.5 μm (Figures 5c, 8j,k and 9a,b). Cells are hollow or filled with featureless opal-A. Their surfaces are smooth or capped with finely granular opal-A spheres (see dominant morphs in Table 1).

These agglomerates dominate the darker laminae of the wavy and palisade laminated fabrics with poor development of fenestrae. Size and shape fit those of some bacteria but also those of single opal-A spheres, precluding any taxonomic recognition. Bacterial communities from circumneutral-alkaline (pH < 8.8) hot spring vent communities (79–83 °C) are dominated by *Aquificales*, the majority of which are chemolithotrophs [89]. As explained for the microbial filaments, cells of the *Thermocrinis ruber* clade can also exhibit some degree of phenotypic plasticity ranging from short rods (up to 5 μm long) in liquid

batch culture to long filaments (even >30 μm long and about 0.5 μm wide) in a flow cultures [90].

Other kinds of thermophilic microorganisms with subspherical shapes are red algae. Eukaryotic cyanidiales are unicellular thermo-acidophilic red algae, which thrive in acidic pH and high temperature conditions around hot springs (Table 1). These unicellular taxa have a relatively simple morphology consisting of subspherical (oval to club- or pear-like shape) thick-walled cells and are the only photosynthetic eukaryotes living under such hostile conditions [91].

5. Iron-Rich Biominerals and Inferred Bacteria

HRTEM observations performed on ultrathin sections of the raw rock, perpendicular to the bedding plane, reveal further information about the presence of nanometer-scale biominerals. They had already illustrated TEM micrographs of cyanobacteria and other bacteria from outflows channels in the Krýsuvík geothermal field showing epicellular and intracellular silica precipitation [37,39,92,93]. However, these biofilm ultrasections were not made on sinter samples, but on partly silicified living biofilms scraped off with sterile scalpels and placed in glutaraldehyde, which revealed that exopolymeric substances (EPS) were iron rich and composed almost exclusively of iron and silica in approximately equal amounts. Our study on silicified microbes under HRTEM has highlighted the ubiquity of goethite crystals embedded in thin organic films or EPS (Figure 9g–j). These show the palisade arrangement of iron-rich needles, somewhat arranged in a fan-shaped way, and in some cases with slightly curved points. The base of these crystals can outline some ovoidal shapes, but they can also occur as disarticulated needle networks and scattered single laths.
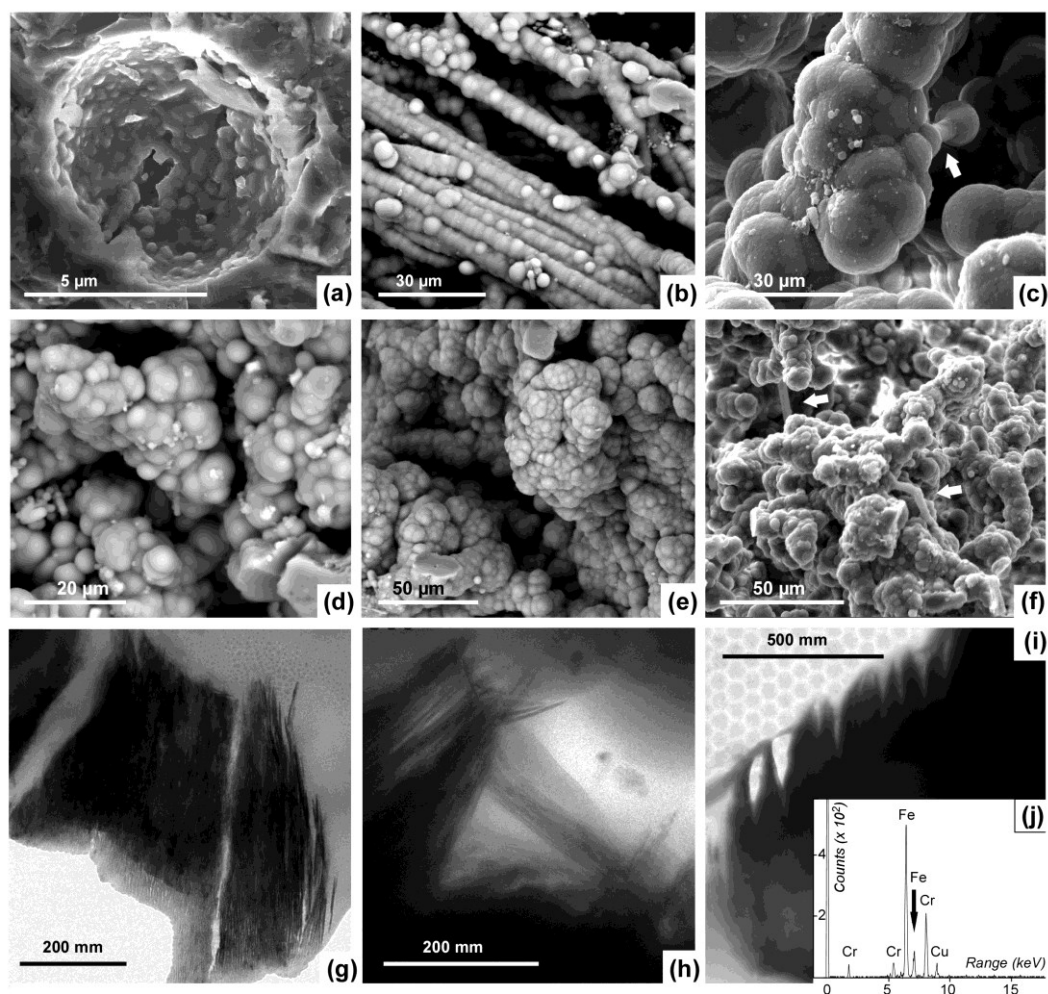
Figure 9. SEM images from samples of the Seltún sinter showing coalescing opal-A spheres and the subsequent disappearance of microbial distinctiveness. (**a**) Broken opal-A sphere showing an internal hollow formed by a crust of smaller spheres, less than 350 nm in diameter. (**b**) Entangled filaments punctuated by opal spheres blurring their microbial distinctiveness. (**c–e**) Botryoidal clusters of opal-A spheres overgrowing microbial filaments; see the neck connecting a mammillated filament with an isolated opal sphere (arrowed). (**f**) Botryoidal mass of opal-A precluding identification of any original microbial remain, except two well-preserved filaments (arrowed) postdating the growth of the botryoidal mass. (**g–i**) High resolution transmission electron microscopy (HRTEM) micrographs of laths and slightly curved needles of goethite (EDX analysis) growing transversally to ellipsoidal outlines of opal-A agglomerates. These mineral associations mimic bacteriomorphs wrapped with iron-rich acicular nanoprecipitates. (**j**) EDS spectra of these iron biominerals embedded in fine exopolymeric substances (EPS) films; Cu and Cr signals are from the supporting grid.

Despite the disability of distinguishing subspherical bacteria from opal-A spheres, the presence of goethite crystals embedded in thin organic films or EPS points to another kind of bacteria. Iron is one of the metals preferentially bound to stems due to the ability of Fe(II)-oxidizing bacteria, such as *Leptothrix* and *Gallionella*, to oxidize ferrous iron as an energy source. Through their metabolic activity, these bacteria commonly become encrusted in ferric hydroxide [37,93–95]. Iron encrusted helical stalks and sheaths are frequently associated with the iron oxide precipitates, indicating the presence of iron oxidizing bacteria [96]. Factors that dictate species dominance in neutrophilic iron-oxidizing bacteria (FeOB) were documented by [97] (Table 1). FeOB are unusual in that they generate large quantities of morphologically distinct, biogenically formed iron oxyhydroxide needles, which can be easily recognized by light microscopy.

6. Preservational Constraints on Silicified Microbes

Opal-A is the first phase to deposit in silica sinters derived from moderately hot (90 °C–60 °C) to warm (60 °C–45 °C) alkali-chloride waters [98,99]. The phase commonly coagulates and/or flocculates from polymeric colloidal states as distinct vitreous microspheres, < 500 nm in diameter. Their size progressively increases by aggregation leading to agglomerated spheres, about 2–10 μm in diameter. The external surfaces are smooth and featureless, although small crescent-shaped depressions are common (Figure 8l). Broken opal-A spheroids show their concentric lamination formed by the amalgamation of spheroids of lesser size (Figure 9a). Larger, globular aggregates and strings (5 to 150 μm long) are common. Larger opal spheres break the overall effect of the images acquired by ESEM. Opal-A agglomerates display a wide range of sizes, the smaller spheroids (<1 μm in diameter) commonly filling the interstices between the larger ones. In some cases, spheroids are connected by a neck or "connected pads" [95] of opal-A less than 1 μm thick (Figure 9c). The connection of neighboring spheroids produces a complex, three-dimensional meshwork.

The main factor governing silica precipitation in geothermal waters is silica saturation, which is a function of pH, temperature, salinity and hydraulic turbulence. The solubility of amorphous silica, in the form of silicic acid monomers, decreases with decreasing temperature. Its solubility does not significantly depend on pH below 7, but it increases with increasing pH above 7 in brine containing sodium. The decrease of monomeric silica concentration is faster at higher stirring speeds, as higher turbulence in the fluid results in a lower mass transfer resistance for the precipitation of monomeric silica onto hard surfaces [100]. High growth rates are attributed primarily to circumneutral pH, high salinity, and medium to high silica contents. In the Reykjanes peninsula, the waters are supersaturated with respect to amorphous silica and measured growth rates are between 200- and 1000-fold higher than other neighboring vents. These parameters concur at Seltún, where spring outflow channels display high silicification backgrounds with growth rates of 304 kg·year^{-1}·m^{-2} or 0.45–0.9 mm·year^{-1} [26,38].

Microbial silicification at Seltún involves three processes: (i) mineral replacement of microbial walls, (ii) coating of microbial walls via permineralization, and (iii) partial-to-complete occlusion of primary porosity. The three processes are controlled by the size and distribution of the precipitated opal-A spheres. The smaller opal-A spheres (<500 nm in

diameter) are typically lesser than the diameter of the subspheroidal and rod-shaped microbes favoring their taxonomic identification. Where the opal-A spheres are more variable in diameter, they commonly merge with each other and display a random distribution [26,101]. After aggregation, larger and composite opal-A spheres, up to 20 μm in diameter, are greater than the diameter of coccoidal and rod-shaped microbes, which become indistinguishable from abiotic precipitates.

Evidence of stepwise silicification includes the thickening of permineralized crusts, manifested by: (i) an increase in the size of opal spheres (Figure 9a); (ii) the less porous and thicker aspect of the crust; and (iii) the decrease in the amount of loosely aggregated opal spheres leading to a corresponding increase in the denser aspect of the aggregates. Progressively, silica spheres coalesced into thicker and dense aggregates with a mammillated external surface (Figure 9c–e). Continued stepwise silicification gave the individual microorganisms an encrusted, mammillated surface relief, which finally resulted to complete embedding of the microorganisms in a siliceous crust and the eventual loss of individual identity. Fluctuations in the degree of silica saturation are reflected by the record of different styles of preservation, with delicately preserved rod-shaped and filamentous microbes, encrusted by mammillated crusts with pores subsequently encrusted by delicately preserved silicified filaments (Figure 9f). Microorganisms play a dominant passive role in silicification yielding heterogeneous nucleation sites for the adsorption of polymeric and/or colloidal silica. As experimental studies have shown that unmineralized cells begin to degrade only a few days after death, delicate preservation of microbial communities suggests that silicification began during life, and continued for some time after their death due to the high reactivity of the newly formed silica [39].

Thickness of silica encrustations directly controls the morphological information from subspherical, rod-shaped, and filamentous microbes. In Table 1, the filamentous morphs are grouped according to their size, lumen size, length/diameter ratio, and presence/absence of septa, whereas the rod-shaped and subspherical morphs are distinguished based on size. The diameters and sizes of silicified microbes are currently larger than those for unsilicified microbes. Their ranges reflect variations in the thickness of opal-A crusts.

7. Biomarker Analysis

In order to test the biological affinity of the organic matter preserved in the silicified microbial sinters from Seltún, the lipid biomarker composition was analyzed in paired samples from each fabric, distinguishing textures (light vs. dark laminae in the wavy and palisade laminated fabric) and the setting of samples (meanders vs. pond margins). Samples were selected based on the pristine preservation of silicified microbes, avoiding mammillated networks, secondary microbial colonizers of open pores, and partly silicified remains. The corresponding samples contain a variety of lipid biomarkers, which can be used to tentatively infer the microbial community composition. The sinters generally contain varying contributions of (i) *n*-fatty acids (e.g., C_{14} to C_{30}, including $C_{16:0}$, $C_{18:0}$, $C_{18:1}$, and 3-OH-C_{14}), some of them combined as fatty acid esters (such as ester-glycerol C_{16}), and branched fatty acids (*iso/anteiso* C_{15} and C_{17}); (ii) *n*-alcohols (C_{16} to C_{30}); (iii) an isoprenoid glycerol diether (archaeol) and non-isoprenoid monoalkyl glycerol ethers (with C_{18}, C_{20}cyclopropyl, and C_{20} alkyl chains) and dialkyl glycerol diethers (with C_{16}/C_{18}, C_{18}/C_{18}, C_{18}/C_{20}cyclopropyl, C_{18}/C_{20}, C_{20}cyclopropyl/C_{20}cyclopropyl, and C_{20}/C_{20}cyclopropyl-dialkyl combinations); and (iv) a hopanoid (bacteriohopanetetrol) (Figure 10). Some sinters contain compounds that are specific to higher plants, such as *n*-alkanes (C_{27}, C_{29}, C_{31}, and C_{33}), a polycyclic terpene phytosteroid (β-sitosterol) and pentacyclic terpenoids (β-amyrin, friedelin, a friedelin-derivative and D-Friedoolean-14-en-3-one). Their presence points to an input of plant material during silicification.
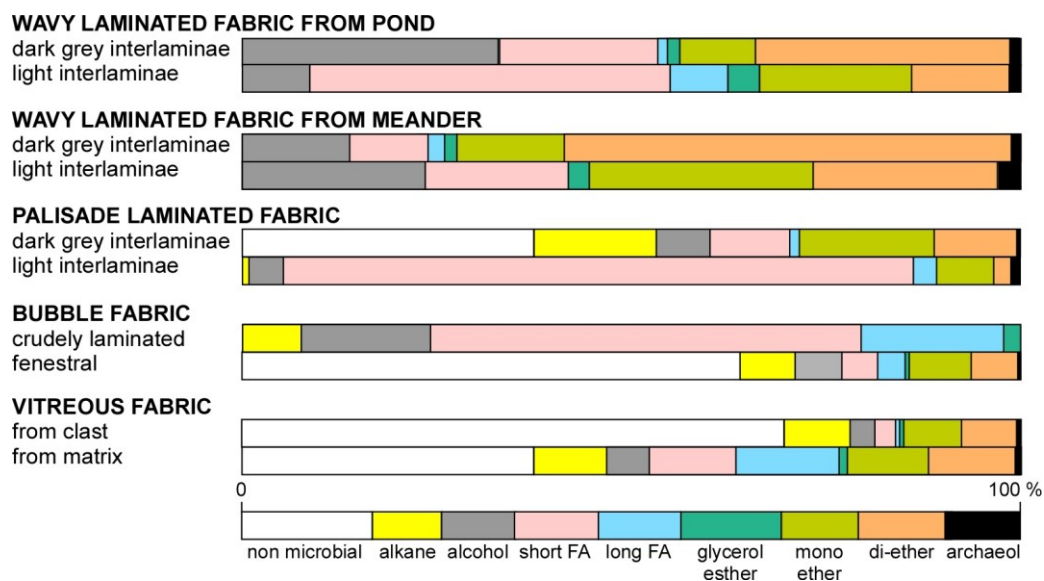
WAVY LAMINATED FABRIC FROM POND
dark grey interlaminae
light interlaminae

WAVY LAMINATED FABRIC FROM MEANDER
dark grey interlaminae
light interlaminae

PALISADE LAMINATED FABRIC
dark grey interlaminae
light interlaminae

BUBBLE FABRIC
crudely laminated
fenestral

VITREOUS FABRIC
from clast
from matrix

0   100 %

non microbial   alkane   alcohol   short FA   long FA   glycerol esther   mono ether   di-ether   archaeol

Figure 10. Relative abundance of main biomarkers from different fabrics and textures.

The detection of archaeol in all samples indicates the presence of archaeal populations in all the sinters. In geothermal environments, archaeol is mainly related to *Sulfolobales* and/or *Thermophilum*-like populations [15,17,102–104]. Similarly, dialkyl glycerol diethers, common in all but one samples, are predominant membrane lipids in some thermophilic bacterial species [17,104], including *Aquificales* [14,103,105], *Ammonifex* [106] and *Thermodesulfobacterium* [107]. Monoalkyl glycerol ethers are associated with these diethers [105,107], among which C_{18} and C_{20} monoethers (the most abundant at Seltún) are inferred to derive largely from *Aquificales* [15,102].

Fatty acids (FAs) are key constituents of bacterial and eukaryotic membranes and likely derive from multiple sources. Nevertheless, a broad source attribution can be made. Low-molecular weight (LMW) fatty acids have a range of potential sources, although the dominance of C_{14}–C_{18} FAs suggests that they have a mainly bacterial origin [104]. More specifically, LMW FAs, such as $C_{16:0}$, $C_{16:1}$, $C_{18:0}$, and $C_{18:1}$ can be linked to *Aquificales* sources [14], while branched fatty acids (*i/a*-$C_{15:0}$ and *i/a*-$C_{17:0}$) can derive from diverse sources including sulfate-reducing bacteria, Gram-positive bacteria and *Thermodesulfobacteriales* [107–110]. The concurrence with allochthonous plant material can be responsible for an elevated FA abundance, in particular FAs with chain lengths of C_{20} and longer; C_{19}-C_{20} fatty acids have also been identified in a variety of *Aquificales* cultures [14]. Hydroxy (β-OH) FAs are associated with both lipopolysaccharides of Gram negative bacteria and fatty acyl parts of phospholipid FAs [111], becoming dominant in some stromatolitic sinters (e.g., *n*-$C_{14:0}$, β-OH acids) [112]. Furthermore, $C_{16:0}$ and $C_{18:1}$ are frequently found in phototrophic organisms such as cyanobacteria and green algae [89], and $C_{16:0}$, $C_{16:1}$, $C_{18:0}$, and $C_{18:1}$ FAs are also produced by *Phormidium* mats [110].

Although the *iso*- and *anteiso*- C_{157} and C_{17} FAs have been found in cyanobacterial mats [113,114], only the sinter with palisade laminated fabric contained bacteriohopanetetrol, a biomarker often found in, but not unique to, cyanobacteria [115]. Other known cyanobacteria biomarkers, such as specific *n*-alkenes and monomethyl alkanes [15,17,116,117], as well as several glycolipid diacylglycerols and a phosphatidylglycerol [118], have not been detected in the Seltún sinters despite the recognition of cyanobacteria in the SEM photographs.

In summary, wavy laminated fabrics from pond margins comprise fatty acids, mono- and dialkyl glycerol (di)ethers, C_{18} and C_{20} alcohols, mono-acyl glycerol esters, and small traces of 10-methyl branched C_{16} and C_{18} fatty acids and archaeol, indicative of intergrowths of cyanobacteria, *Aquificales* and sulfate reducing and methanogenic archaea. In

contrast, wavy laminated fabrics from abandoned meanders and palisade laminated fabrics from ponds differ in the branched fatty acids and the presence vs. absence of bacteriohopanetetrol, pointing to a different microbial community composition with possible contributions from different cyanobacteria. Biomarkers in bubble and vitreous fabrics are less diverse and comprise undiagnostic fatty acids and mono- and dialkyl glycerol ethers (Figure 10).

The near absence (<1%) of cyanobacteria biomarkers, compared to the clearly recognizable filaments on the SEM images, indicating their abundance, is remarkable. Their scarcity contrasts with their relative abundance yielded by biomarker analysis in El Tatio (Chile) and the Taupo Volcanic Zone (New Zealand) sinters [119], which are focused on the apolar fraction (comprising about 1–2% of all biomarkers) with high C_{17} alkane peaks, whereas in our analysis the alkanes were dominated by plant-derived (C_{27}–C_{33}) "contaminants". The scarcity of cyanobacteria diagnostic biomarkers at Seltún may be explained by differences in the preservation of the organic carbon in the silicified mats. The organic carbon fixed by cyanobacteria may have been consumed by later bacteria and archaea leaving a predominately sulfate reducing bacterial biomarker overprint, detected in the sinters. Alternatively, the cyanobacteria in our samples did not produce the documented diagnostic biomarkers, and only contained those shared with other microbes, such as C_{16} and C_{18} saturated and unsaturated FAs. The absence of monoalkyl glycerol monoethers and other cyanobacterial diagnostic biomarkers is suggested as characteristic of inactive sinters [17]. Indeed, in our inactive sinters, none of the aforementioned cyanobacterial biomarkers were observed, except for a bacteriohopanetetrol in the palisade laminated fabric. In contrast, the abundant mono-alkyl glycerol ethers derived from sulfate reducing bacteria, and the coinciding prominent presence of dialkyl glycerol diethers combined with the significant presence of elemental sulfur suggest that these bacteria thrive well in the Seltún sinters.

8. Carbon Isotopic Signatures of Lipid Biomarkers

To verify the carbon source of the microbes that produced the biomarkers, their stable carbon isotopic composition was determined. For the dialkyl glycerol diethers, $\delta^{13}C$ values range between −20.9 and −27.8‰ (averaging at −26.4‰), for monoethers between −24 and −27‰ (averaging at −25.2‰), for free alcohols between−24.6 and −32.9‰ (averaging at −26.9‰), for fatty acids between −22.7 and −30.6‰ (averaging at 28.8‰), and for archaeol between −26.7 and −30.8‰ (averaging at −27.7). Plant-derived alkanes and pentacyclic terpenoids show more uniform and depleted values ranging from −28.2 to −31.2‰ (averaging at 30‰; see Table 2). The $\delta^{13}C$ values of the biomarkers in the wavy (in pond) and bubble fabrics have a much wider range (8.5–9.9‰) than those of the wavy (in meander), palisade and vitreous fabrics (6.1–7‰).

Table 2. $\delta^{13}C$ isotopic values of biomarkers in samples from wavy laminated (pond margin and meander), vitreous, palisade, and bubble fabrics.

Fabric / Compound	Wavy (in Pond)				Wavy (in Meander)		Bubble	Palisade	Vitreous		
Dialkyl glycerol diethers											
C_{18}/C_{18}	−26.3	−25.3	−25.4	−24.9	−24.9	−24.1	−26.3		−26.0	−26.3	−25.8
$C_{18}/cycpropC_{20}$	−25.0	−24.9	−24.7	−24.2	−23.4	−24.0	−25.7		−25.9	−25.5	−24.7
C_{18}/C_{20}	−25.8	−26.3	−25.5	−25.1	−27.0	−20.9	−25.5		−27.6	−27.6	−27.7
$cyclopropC_{20}/cyclopropC_{20}$			−23.0		−22.2	−24.9		−24.2			
$C_{20}/cyclopropC_{20}$			−25.1		−23.9	−25.2		−25.9			
Archaeol			−26.7	−27.2	−26.8	−27.8		−27.1			−30.8
Monoalkyl glycerol ethers											
C_{18}	−25.6	−24.6	−24.5	−25.0	−25.9	−24.7	−24.6		−24.5	−24.9	−24.8
C_{20}	−26.5	−25.3	−27.0	−24.8	−25.6	−24.5	−25.9		−24.0	−25.3	−26.0
n-Alcohols											

C$_{18}$	−29.9	−26.4	−24.9	−27.0	−25.3	−25.3			−25.4	
C$_{20}$	−32.9	−31.1	−24.8	−27.2	−24.6	−26.1			−26.6	
n-Fatty acids										
C16:1	−28.4	−30.6								
C16	−27.8	−30.0					−30.6	−25.4	−27.5	
C18:1	−30.2	−30.1					−28.8	−26.7		
C18	−30.6	−29.8					−22.7	−24.9	−26.8	
Pentacyclic terpenoids										
Friedolean-4-en-3-one						−31.2			−31.1	−30.0
Friedelin						−30.0			−28.2	−29.5
C$_{29}$ alkane										−30.2
C$_{31}$ alkane										−29.8

The δ13C values of the referred biomarkers indicate that their producers did not use methane as carbon sources. The microbial compounds were slightly more depleted than those derived from plants, and suggest that their producers used either directly, or indirectly via cyanobacterial debris, dissolved inorganic carbon (DIC = dissolved CO_2 + HCO_3^- + $CO_3^=$) as primary carbon source.

In general, the compound specific δ13C values decrease downstream outflow channels, and is similar to what has been reported in other case studies [18,120], with heavier values closer to vents (e.g., in the abandoned meanders) and depleted values in ponds. A relatively high 13C content could also be related to CO_2 fixation pathways different from the Calvin cycle, as reported for the non-sulfur bacterium *Chloroflexus*, generating biomarkers that are isotopically enriched relative to lipids typical of cyanobacteria [121], which may also explain the 13C isotopic values obtained for the palisade laminated fabric from the pond margin.

In recent years, numerous measurements on DIC isotopes in Icelandic waters (surface, and cold and thermal groundwater) have been performed. The dataset spans geographically all parts of Iceland and reflects wide ranges of δ13C values, from +2 to −26‰. In the Krýsuvík geothermal field, δ13C values of DIC in geothermal waters range from −1.5 to −16.8‰ [122]. The origin of the thermal waters has been traced by deuterium to the mountainous areas, where the isotopic composition of local precipitation is similar to that of thermal waters. The water is assumed to flow along the Krýsuvík fissure swarms. The thermal systems are all considered to be convection systems drawing heat from the roots of old central volcanoes in the area [123]. The δ13C of Icelandic bedrock is about −4‰, Icelandic plants and soils −25‰ and atmospheric δ13C value of −7‰ [124], as result of which, the groundwater experiencing a long term contact with organic matter would become progressively depleted in 13C.

9. Environmental Distribution

The fabrics and textures reported at Seltún should be explained as a result of episodes of stepwise silicification events, controlled by fluctuations in hydrodynamic features and microbial production. Hot-spring waters are saturated with respect to amorphous silica at the sites of discharge, so precipitation of opal-A can be related to rapid cooling and evaporation [38,39]. As we move away from the spring and stream vents and downstream, the water progressively cools (from 96 °C to 26 °C) and pH increases (from 1.7 to 7.7) controlling the record of microbial fabrics and textures. The fabric arrangement differs with increasing distance from vent sources, reflecting how temperature, pH, silica concentration, and turbulence decrease (Figure 11a,b).
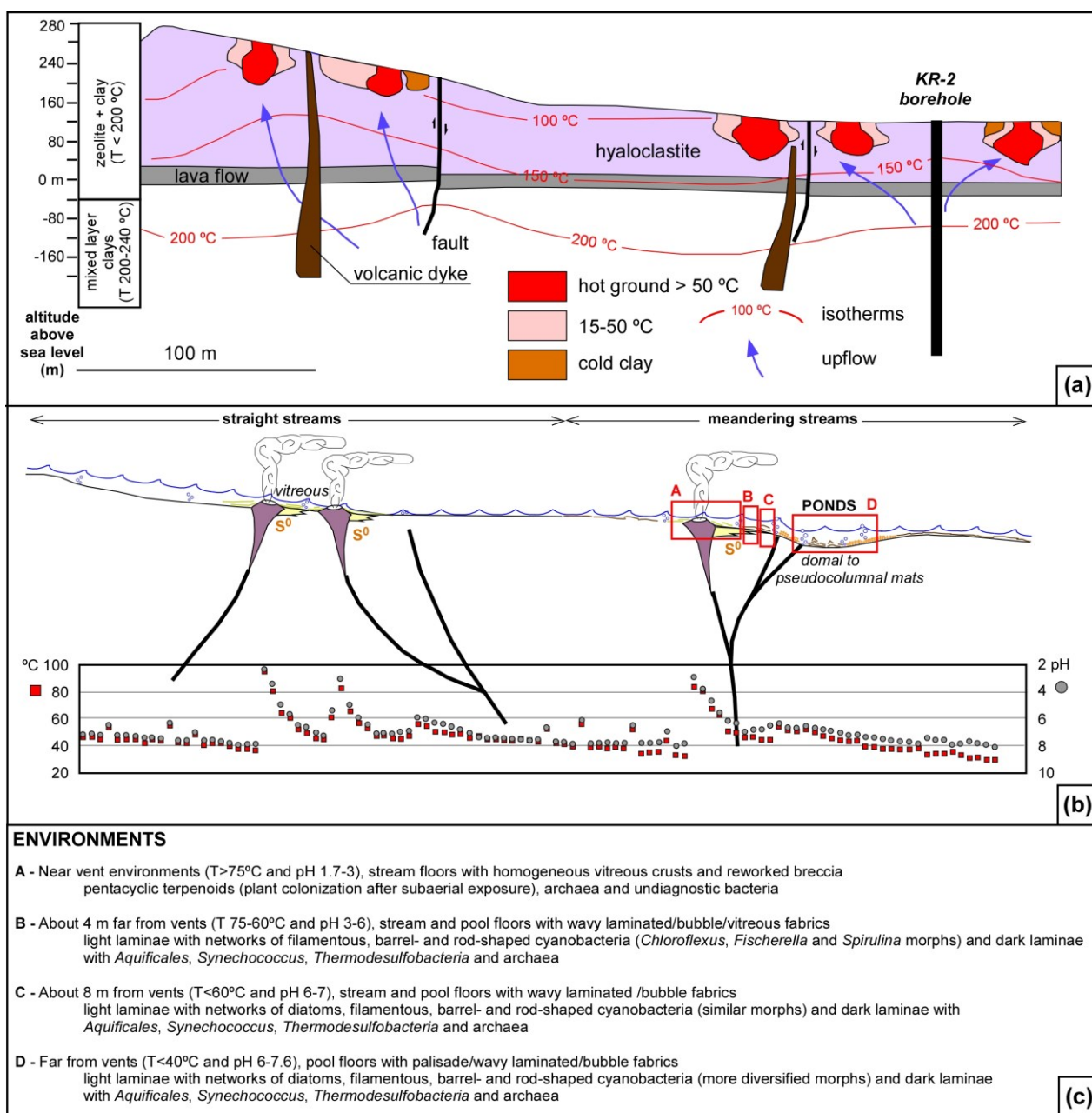
Figure 11. Schematic diagram of the Seltún area in the Krýsuvík geothermal. (**a**) Geothermal model for the Seltún area; modified from [30]. (**b**) Idealized distribution of fabrics described in the text affected by sharp modifications in temperature and pH conditions of surface waters (measured with a Milwaukee Pro + pH meter; 26 August 2016) controlled by setting of dykes and faults; S^0 abundant native sulfur. (**c**) Summary of environments and their microbial sinters at Seltún.

Some distinct fabric trends can be documented with increasing distance from the main hot springs, which are surrounded by vitreous fabrics progressively replaced by wavy laminated and bubble fabrics farther from vents. The ponds comprise intergrowths of these fabrics with the palisade laminated fabrics, which would reflect more stable physico-chemical conditions. High topographic gradients associated with turbulent waters are not favorable for thick sinter deposits, which are dominated by millimeter-thick crusts with vitreous fabrics. In contrast, lower topographic gradients are favorable for precipitation of centimeter-thick crusts.

The wavy laminated fabric displays a distinct textural alternation: light/dark grey sinter couplets, reflecting cyclic alternations of organic matter content and dominance of cyanobacterial vs. bacterial–archaeal consortia. This cyclic repetition may be related to cyclic changes in temperature and pH, which should not be associated with any cyclicity of

the hydrothermal activity, but likely with annual (winter–summer) temperature oscillations (ca. 15 °C–20 °C in the study area). The palisade laminated fabric also shows a textural alternation controlled by the laminar-to-upright arrangement of microbial filaments. This fabric is likely controlled by a ''pulse–pause'' style of sheet flow that is sensitive to hot spring output conditions and lateral flow-path shifts, and currently occurs in quiet ponds [65]. The change in filament orientation seems intimately linked to the wet–dry cycles of the sinter [69].

In summary, a replacement of sinter fabrics with increasing distance from vent sources can be documented (Figure 11c).

(i) In the vicinity of vents, high temperature (>75 °C) and acid (pH 1.7–3) stream floors are encrusted with homogeneous vitreous crusts, up to 2 cm thick. Microbial casts are virtually absent but biomarkers reflect the onset of subsidiary archaeal and undiagnostic (fatty acids) bacterial signatures. Pentacyclic terpenoids, related to the colonization of porosity by plants after subaerial exposure, are relatively abundant and points to secondary colonization of porosity after subaerial exposure.

(ii) Moderately high temperature (75 °C–60 °C) and acid (pH 3–6) stream and pool floors are encrusted with biofilms and mats, up to 10 cm thick, exhibiting wavy laminated and bubble fabrics. Their textural couplets show alternations of (i) porous to bubble, light inter-laminae formed by the intergrowth of filamentous cyanobacteria, and other bacteria (including *Chloroflexus* and *Spirulina* morphs); and (ii) dark grey inter-laminae dominated by barrel-shaped (*Fischerella* morph) to rod-shaped (*Synechococcus*-like morph) organisms. Rod-shaped to subspherical microbes, less than 5 μm in size and similar in shape and size to opal spheres, cannot be taxonomically recognized. The biomarkers of the dark grey inter-laminae allow recognition of populations dominated by *Aquificales* associated with subsidiary Thermodesulfobacteria, sulfate-reducing bacterial, and archaeal (*Sulfolobales* and/or *Thermophilum*-like populations) signatures. The concentration of sulfide in waters sourced from solfataric vents in Iceland directly controls the *Aquificales*/cyanobacterial ratio [125]: *Chloroflexus* is the dominant mat organism in low-sulfide springs below 70 °C, whereas *Aquificales* become dominant in high-sulfide springs at similar temperatures.

(iii) Below 60 °C, cyanobacteria and other photosynthetic bacteria commonly form wavy-laminated and bubble fabrics with similar biomarkers. The morphology of the cyanobacterial network displays wider ranges and reflects the diversification of cyanobacterial populations. Although eukaryotic algae colonize substrates at temperatures <60 °C, their distinct biomarkers have not been recognized.

(iv) The palisade laminated fabric dominates the floors of low temperature (<40 °C), circumneutral ponds. Palisade fabrics are associated with the growth of sheathed, filamentous cyanobacteria [50,66]. At water temperatures below 35 °C, the cyanobacterium *Calothrix* is typically observed to be responsible for palisade fabric formation in sinter deposits [10,66,87,126].

10. Astrobiological Implications

On Earth, aging of silica sinter deposits is accompanied by dehydration, increase in density and loss of porosity [49]. Preservation of microbial fossils entombed within silica precipitates is favored by host rocks resistant to chemical weathering, such as cherts. However, during increasing burial depth, cherts are subjected to progressively higher temperatures and pressures, which destroy primary biogenic signatures. Above 80 °C, organic matter begins to undergo thermal cracking (catagenesis), liberating the most volatile constituents and leaving behind only refractory components (kerogen) with modified molecular and isotopic composition. Under low-grade metamorphic conditions (ca. 150 °C–200 °C), microbial evidence becomes more difficult to interpret or is lost completely.

However, hydrated silica occurrences associated with sulfide precipitates have been identified in situ by rovers and orbiting spacecrafts on Mars, which have been interpreted as a result of sinter deposition from hot springs [6,127,128]. Unlike on Earth, the amorphous hydrated opal form (opal-A) is not transformed to paracrystalline forms (Opal-

C/CT) and fully crystalline anhydrous quartz, but Opal-A seemingly persists on Mars due to extreme aridity conditions [129].

As documented in this paper, sinter fabrics and textures are mainly controlled by microbial communities, influencing the preservation of microbially induced facies at macro-, meso- and microscales. Recognition of these bio-mediated sinter multiscales is key to understand the significance of hot spring deposits on Mars. The microbial diversity of sinter deposits varies greatly as a function of physical, chemical and biological factors that relate to the functional requirements of life in that environment and/or the specific organisms that first successfully colonize these substrates. As documented in this paper, gradients in both physical parameters, such as temperature, pH, and sulfur content, control multi-scale variations in microbial diversity. Therefore, a strategy for sample collection on Mars seems necessary based on the heterogeneity of microbial fabrics and textures in their analogous silica sinters on Earth.

11. Conclusions

This work provides a detailed description of petrographic textures, silicified microbes, lipid biomarkers, and their carbon isotopes of several siliceous sinter fabrics from the Krýsuvík geothermal field, Iceland. Water chemistry with variable pH values (1.5–7.9) and silica content (50–700 ppm), reflecting different springs with variable temperatures (30 °C–95 °C), is primarily controlling modifications in the microbial consortia, which influenced the sinter fabrics and textures. The extremely fast silica precipitation rates in the near vent environments, with $T > 75$ °C and pH 1.7–3, controlled precipitation of stream floors with homogeneous vitreous crusts that prevented the taxonomic identification of microbial morphotypes. About 4 m far from the vents and beyond ($T < 60$ °C and pH 6–7.6), microbial sinters occur in stream meanders and pond margins with wavy laminated, bubble and palisade laminated fabrics. The laminated fabrics display three common textures characterized by (i) onlapping packages of convex-up microbial laminae composed of sparsely packed meshworks of filamentous microbes and subsidiary coccoids; (ii) flat-domal-columnar laminae formed by densely interwoven, flat-lying filaments that display gradual modifications in porosity, becoming both laterally and vertically, bubble fabrics; the darker layers are composed of densely packed rod-shaped and coccoidal-dominated clusters, with subsidiary filaments, arranged subparallel to the lamination, but, where the clusters misplace their subparallel arrangement, they form highly-porous (bubble-style), filament-coccoid meshworks; (iii) palisade laminae of upward branching dendroids, formed by loosely interwoven, branching and non-branching filament bundles. The morphology of the filamentous microbes mimics those characteristic of cyanobacteria, whereas the rod-shaped and coccoid shapes are referred to bacteriomorphs. Iron oxide/hydroxide laths occur as biominerals attached to the EPS of filaments, visible by HRTEM, and point to the influence of Fe(II)-oxidizing bacteria.

Wavy laminated fabrics from pond margins have yielded free $C_{16:1}$, $C_{16:0}$, $C_{18:1}$, and C_{18} fatty acids, mono- and dialkyl glycerol diethers, C_{18} and C_{20} alcohols, monoacyl glycerol monoesters, and small traces of 10-methyl branched C_{16} and C_{18} fatty acids, indicative of sulfate reducing and methanogenic archaea. Wavy laminated fabrics from abandoned meanders and palisade laminated fabrics share many biomarkers, but differ in the presence vs. absence of bacteriohopanetetrol and branched fatty acids (*iso-* and *anteiso* C_{15} and C_{17}). Biomarkers in bubble and vitreous fabrics are less diverse and comprise undiagnostic fatty acids and mono- and dialkyl glycerol diethers, indicative of sulfate reducers. Archaeol is subsidiary in all the fabrics. The $\delta^{13}C$ values of the biomarkers indicate that the microbial community was primarily sourced by DIC, and not methane. Biomarker-specific $\delta^{13}C$ values in the wavy (in pond) and bubble fabrics display a much wider range than those of the wavy (in meander), palisade and vitreous fabrics. Stable carbon isotope values decrease downstream outflow channels, with heavier values in meanders close to vents and more depleted values in ponds.

References

1. Allwood, A.C.; Walter, M.R.; Kamber, B.S.; Marshall, C.P.; Burch, I.W. Stromatolite reef from the Early Archaean era of Australia. *Nat. Cell Biol.* **2006**, *441*, 714–718, doi:10.1038/nature04764.
2. Noffke, N.; Eriksson, K.A.; Hazen, R.M.; Simpson, E.L. A new window into Early Archean life: Microbial mats in Earth's oldest siliciclastic tidal deposits (3.2 Ga Moodies Group, South Africa). *Geology* **2006**, *34*, 253, doi:10.1130/g22246.1.
3. Schopf, J.W.; Kudryavtsev, A.B.; Czaja, A.D.; Tripathi, A.B. Evidence of Archean life: Stromatolites and microfossils. *Precambrian Res.* **2007**, *158*, 141–155, doi:10.1016/j.precamres.2007.04.009.
4. Djokic, T.; Van Kranendonk, M.J.; Campbell, K.A.; Walter, M.R.; Ward, C.R. Earliest signs of life on land preserved in ca. 3.5 Ga hot spring deposits. *Nat. Commun.* **2017**, *8*, 15263, doi:10.1038/ncomms15263.
5. Dodd, M.S.; Papineau, M.S.D.D.; Grenne, T.; Slack, J.F.; Rittner, M.S.D.D.P.M.; Pirajno, F.; O'Neil, J.; Little, C.T.S. Evidence for early life in Earth's oldest hydrothermal vent precipitates. *Nat. Cell Biol.* **2017**, *543*, 60–64, doi:10.1038/nature21377.
6. Squyres, S.W.; Arvidson, R.E.; Ruff, S.; Gellert, R.; Morris, R.V.; Ming, D.W.; Crumpler, L.; Farmer, J.D.; Marais, D.J.D.; Yen, A.; et al. Detection of Silica-Rich Deposits on Mars. *Science* **2008**, *320*, 1063–1067, doi:10.1126/science.1155429.
7. Ruff, S.W.; Farmer, J.D.; Calvin, W.M.; Herkenhoff, K.E.; Johnson, J.R.; Morris, R.V.; Rice, M.S.; Arvidson, R.E.; Bell, J.F.; Christensen, P.R.; et al. Characteristics, distribution, origin, and significance of opaline silica observed by the Spirit rover in Gusev crater, Mars. *J. Geophys. Res. Space Phys.* **2011**, *116*, doi:10.1029/2010je003767.
8. Damer, B.; Deamer, D. Coupled Phases and Combinatorial Selection in Fluctuating Hydrothermal Pools: A Scenario to Guide Experimental Approaches to the Origin of Cellular Life. *Life* **2015**, *5*, 872–887, doi:10.3390/life5010872.
9. Ruff, S.W.; Farmer, J.D. Silica deposits on Mars with features resembling hot spring biosignatures at El Tatio in Chile. *Nat. Commun.* **2016**, *7*, 13554, doi:10.1038/ncomms13554.
10. Konhauser, K.O.; Jones, B.; Reysenbach, A.-L.; Renaut, R.W. Hot spring sinters: Keys to understanding Earth's earliest life forms. *Can. J. Earth Sci.* **2003**, *40*, 1713–1724, doi:10.1139/e03-059.
11. Gangidine, A.; Havig, J.R.; Fike, D.A.; Jones, C.; Hamilton, T.L.; Czaja, A.D. Trace Element Concentrations in Hydrothermal Silica Deposits as a Potential Biosignature. *Astrobiology* **2020**, *20*, 525–536, doi:10.1089/ast.2018.1994.
12. Gangidine, A.; Walter, M.R.; Havig, J.R.; Jones, C.; Sturmer, D.M.; Czaja, A.D. Trace Element Concentrations Associated with Mid-Paleozoic Microfossils as Biosignatures to Aid in the Search for Life. *Life* **2021**, *11*, 142, doi:10.3390/life11020142.
13. Lindahl, T. Instability and decay of the primary structure of DNA. *Nat. Cell Biol.* **1993**, *362*, 709–715, doi:10.1038/362709a0.
14. Jahnke, L.L.; Eder, W.; Huber, R.; Hope, J.M.; Hinrichs, K.-U.; Hayes, J.M.; Marais, D.J.D.; Cady, S.L.; Summons, R.E. Signature Lipids and Stable Carbon Isotope Analyses of Octopus Spring Hyperthermophilic Communities Compared with Those ofAquificales Representatives. *Appl. Environ. Microbiol.* **2001**, *67*, 5179–5189, doi:10.1128/aem.67.11.5179-5189.2001.
15. Pancost, R.D.; Pressley, S.; Coleman, J.M.; Benning, L.G.; Mountain, B.W. Lipid biomolecules in silica sinters: Indicators of microbial biodiversity. *Environ. Microbiol.* **2005**, *7*, 66–77, doi:10.1111/j.1462-2920.2004.00686.x.
16. Kaur, G.; Mountain, B.W.; Pancost, R.D. Microbial membrane lipids in active and inactive sinters from Champagne Pool, New Zealand: Elucidating past geothermal chemistry and microbiology. *Org. Geochem.* **2008**, *39*, 1024–1028, doi:10.1016/j.orggeochem.2008.04.016.
17. Kaur, G.; Mountain, B.W.; Stott, M.B.; Hopmans, E.C.; Pancost, R.D. Temperature and pH control on lipid composition of silica sinters from diverse hot springs in the Taupo Volcanic Zone, New Zealand. *Extremophiles* **2015**, *19*, 327–344, doi:10.1007/s00792-014-0719-9.
18. Schubotz, F.; Meyer-Dombard, D.R.; Bradley, A.S.; Fredricks, H.F.; Hinrichs, K.-U.; Shock, E.L.; Summons, R.E. Spatial and temporal variability of biomarkers and microbial diversity reveal metabolic and community flexibility in Streamer Biofilm Communities in the Lower Geyser Basin, Yellowstone National Park. *Geobiology* **2013**, *11*, 549–569, doi:10.1111/gbi.12051.
19. Mata, S.A.; Harwood, C.L.; Corsetti, F.A.; Stork, N.J.; Eilers, K.; Berelson, W.M.; Spear, J.R. Influence of Gas Production and Filament Orientation on Stromatolite Microfabric. *Palaios* **2012**, *27*, 206–219, doi:10.2110/palo.2011.p11-088r.
20. Pepe-Ranney, C.; Berelson, W.M.; Corsetti, F.A.; Treants, M.; Spear, J.R. Cyanobacterial construction of hot spring siliceous stromatolites in Yellowstone National Park. *Environ. Microbiol.* **2012**, *14*, 1182–1197, doi:10.1111/j.1462-2920.2012.02698.x.

21. Bickford, M.E. The Web of Geological Sciences: Advances, Impacts, and Interactions. In *Geological Society of America Special Papers*; Geological Society of America: Boulder, CO, USA, 2013.

22. Phoenix, V.R.; Adams, D.G.; Konhauser, K.O. Cyanobacterial viability during hydrothermal biomineralisation. *Chem. Geol.* **2000**, *169*, 329–338, doi:10.1016/s0009-2541(00)00212-6.

23. Yee, N.; Phoenix, V.R.; Konhauser, K.O.; Benning, L.G.; Ferris, F. The effect of cyanobacteria on silica precipitation at neutral pH: Implications for bacterial silicification in geothermal hot springs. *Chem. Geol.* **2003**, *199*, 83–90, doi:10.1016/s0009-2541(03)00120-7.

24. Menzel, P.; Gudbergsdóttir, S.R.; Rike, A.G.; Lin, L.; Zhang, Q.; Contursi, P.; Moracci, M.; Kristjansson, J.K.; Bolduc, B.; Gavrilov, S.; et al. Comparative Metagenomics of Eight Geographically Remote Terrestrial Hot Springs. *Microb. Ecol.* **2015**, *70*, 411–424, doi:10.1007/s00248-015-0576-9.

25. Tobler, D.J.; Stefánsson, A.; Benning, L.G. In-situ grown silica sinters in Icelandic geothermal areas. *Geobiology* **2008**, *6*, 481–502, doi:10.1111/j.1472-4669.2008.00179.x.

26. Tobler, D.J.; Benning, L.G. Bacterial diversity in five Icelandic geothermal waters: Temperature and sinter growth rate effects. *Extremophiles* **2011**, *15*, 473–485, doi:10.1007/s00792-011-0378-z.

27. Hersir, G.P.; Árnason, K.; Vilhjálmsson, A.M.; Saemundsson, K.; Ágústsdóttir, Þ.; Friðleifsson, G. Ómar Krýsuvík high temperature geothermal area in SW Iceland: Geological setting and 3D inversion of magnetotelluric (MT) resistivity data. *J. Volcanol. Geotherm. Res.* **2020**, *391*, 106500, doi:10.1016/j.jvolgeores.2018.11.021.

28. Franzson, H.; Zierenberg, R.A.; Schiffman, P. Chemical transport in geothermal systems in Iceland. *J. Volcanol. Geotherm. Res.* **2008**, *173*, 217–229, doi:10.1016/j.jvolgeores.2008.01.027.

29. Markússon, S.H.; Stefánsson, A. Geothermal surface alteration of basalts, Krýsuvík Iceland—Alteration mineralogy, water chemistry and the effects of acid supply on the alteration process. *J. Volcanol. Geotherm. Res.* **2011**, *206*, 46–59, doi:10.1016/j.jvolgeores.2011.05.007.

30. Mawejje, P. Geothermal exploration and geological mapping at Seltún, Krýsuvík geothermal field, Reykjanes Peninsula, SW-Iceland. *Geotherm. Train. Programme Rep.* **2007**, *12*, 1–276.

31. Ármannsson, H. The fluid geochemistry of Icelandic high temperature geothermal areas. *Appl. Geochem.* **2016**, *66*, 14–64, doi:10.1016/j.apgeochem.2015.10.008.

32. Gudjónsdóttir, S.R.; Ilyinskaya, E.; Hreinsdóttir, S.; Bergsson, B.; Pfeffer, M.A.; Michalczewska, K.; Aiuppa, A.; Óladóttir, A.A. Gas emissions and crustal deformation from the Krýsuvík high temperature geothermal system, Iceland. *J. Volcanol. Geotherm. Res.* **2020**, *391*, 106350, doi:10.1016/j.jvolgeores.2018.04.007.

33. Chung, A.P.; Rainey, F.A.; Valente, M.; Nobre, M.F.; Da Costa, M.S. Thermus igniterrae sp. nov. and Thermus antranikianii sp. nov., two new species from Iceland. *Int. J. Syst. Evol. Microbiol.* **2000**, *50*, 209–217, doi:10.1099/00207713-50-1-209.

34. Hjorleifsdottir, S.; Skirnisdottir, S.; Hreggvidsson, G.; Holst, O.; Kristjansson, J. Species Composition of Cultivated and Noncultivated Bacteria from Short Filaments in an Icelandic Hot Spring at 88 °C. *Microb. Ecol.* **2001**, *42*, 117–125, doi:10.1007/s002480000110.

35. Kvist, T.; Ahring, B.K.; Westermann, P. Archaeal diversity in Icelandic hot springs. *FEMS Microbiol. Ecol.* **2007**, *59*, 71–80, doi:10.1111/j.1574-6941.2006.00209.x.

36. Schultze-Lam, S.; Ferris, F.G.; Konhauser, K.O.; Wiese, R.G. In situ silicification of an Icelandic hot spring microbial mat: Implications for microfossil formation. *Can. J. Earth Sci.* **1995**, *32*, 2021–2026, doi:10.1139/e95-155.

37. Konhauser, K.O.; Ferris, F.G. Diversity of iron and silica precipitation by microbial mats in hydrothermal waters, Iceland: Implications for Precambrian iron formations. *Geology* **1996**, *24*, 323–326, doi:10.1130/0091-7613(1996)0242.3.co;2.

38. Konhauser, K.O.; Phoenix, V.R.; Bottrell, S.H.; Adams, D.G.; Head, I.M. Microbial-silica interactions in Icelandic hot spring sinter: Possible analogues for some Precambrian siliceous stromatolites. *Sedimentology* **2001**, *48*, 415–433, doi:10.1046/j.1365-3091.2001.00372.x.

39. Konhauser, K.O.; Jones, B.; Phoenix, V.R.; Ferris, G.; Renaut, R.W. The Microbial Role in Hot Spring Silicification. *AMBIO* **2004**, *33*, 552–558, doi:10.1579/0044-7447-33.8.552.

40. Petursdottir, S.K.; Hreggvidsson, G.O.; Da Costa, M.S.; Kristjansson, J.K. Genetic diversity analysis of Rhodothermus reflects geographical origin of the isolates. *Extremophiles* **2000**, *4*, 267–274, doi:10.1007/s007920070012.

41. Hreggvidsson, G.O.; Skirnisdottir, S.; Smit, B.; Hjörleifsdottir, S.; Marteinsson, V.T.; Petursdottir, S.; Kristjansson, J.K. Polyphasic analysis of Thermus isolates from geothermal areas in Iceland. *Extremophiles* **2006**, *10*, 563–575, doi:10.1007/s00792-006-0530-3.

42. Sæmundsson, K.; Sigurgeirsson, M.Á.; Friðleifsson, G. Ómar Geology and structure of the Reykjanes volcanic system, Iceland. *J. Volcanol. Geotherm. Res.* **2020**, *391*, 106501, doi:10.1016/j.jvolgeores.2018.11.022.

43. Jóhannesson, H.; Sæmundsson, K. *Geological Map of Iceland, 1:500,000*; Icelandic Institute of Natural History: Reykjavík, Iceland, 1998.

44. Pałgan, D.; Devey, C.W.; Yeo, I.A. Volcanism and hydrothermalism on a hotspot–influenced ridge: Comparing Reykjanes Peninsula and Reykjanes Ridge, Iceland. *J. Volcanol. Geotherm. Res.* **2017**, *348*, 62–81, doi:10.1016/j.jvolgeores.2017.10.017.

45. Fridriksson, T.; Kristjánsson, B.R.; Ármannsson, H.; Margrétardóttir, E.; Ólafsdóttir, S.; Chiodini, G. CO_2 emissions and heat flow through soil, fumaroles, and steam heated mud pools at the Reykjanes geothermal area, SW Iceland. *Appl. Geochem.* **2006**, *21*, 1551–1569, doi:10.1016/j.apgeochem.2006.04.006.

46. Ármannsson, H.; Fridriksson, T.; Kristjánsson, B.R. CO_2 emissions from geothermal power plants and natural geothermal activity in Iceland. *Geothermics* **2005**, *34*, 286–296, doi:10.1016/j.geothermics.2004.11.005.

47. Stefánsson, A.; Hilton, D.R.; Sveinbjörnsdóttir, Á.E.; Torssander, P.; Heinemeier, J.; Barnes, J.D.; Ono, S.; Halldórsson, S.A.; Fiebig, J.; Arnórsson, S. Isotope systematics of Icelandic thermal fluids. *J. Volcanol. Geotherm. Res.* **2017**, *337*, 146–164, doi:10.1016/j.jvolgeores.2017.02.006.

48. Konhauser, K.O.; Phoenix, V.R.; Bottrell, S.H.; Adams, D.G.; Head, I.M. Microbial-silica interactions in modern hot spring sinter. In *Geochemistry of the Earth Surface*; Ármannsson, H., Ed.; Balkema: Rotterdam, The Netherlands, 1999; pp. 263–266.

49. Herdianita, N.R.; Browne, P.R.L.; Rodgers, K.A.; Campbell, K.A. Mineralogical and textural changes accompanying ageing of silica sinter. *Miner. Deposita* **2000**, *35*, 48–62, doi:10.1007/s001260050005.

50. Lynne, B.Y.; Campbell, K.A. Diagenetic transformations (opal-A to quartz) of low- and mid-temperature microbial textures in siliceous hot-spring deposits, Taupo Volcanic Zone, New Zealand. *Can. J. Earth Sci.* **2003**, *40*, 1679–1696, doi:10.1139/e03-064.

51. Lynne, B.Y.; Campbell, K.A. Morphologic and Mineralogic Transitions from Opal-A to Opal-CT in Low-Temperature Siliceous Sinter Diagenesis, Taupo Volcanic Zone, New Zealand. *J. Sediment. Res.* **2004**, *74*, 561–579, doi:10.1306/011704740561.

52. Guidry, S.A.; Chafetz, H.S. Depositional Facies and Diagenetic Alteration in a Relict Siliceous Hot-Spring Accumulation: Examples from Yellowstone National Park, U.S.A. *J. Sediment. Res.* **2003**, *73*, 806–823, doi:10.1306/022803730806.

53. Guidry, S.A.; Chafetz, H.S. Siliceous shrubs in hot springs from Yellowstone National Park, Wyoming, U.S.A. *Can. J. Earth Sci.* **2003**, *40*, 1571–1583, doi:10.1139/e03-069.

54. Lynne, B.Y.; Campbell, K.A.; Moore, J.; Browne, P. Diagenesis of 1900-year-old siliceous sinter (opal-A to quartz) at Opal Mound, Roosevelt Hot Springs, Utah, U.S.A. *Sediment. Geol.* **2005**, *179*, 249–278, doi:10.1016/j.sedgeo.2005.05.012.

55. Jones, B.; Renaut, R.W. Microstructural changes accompanying the opal-A to opal-CT transition: New evidence from the siliceous sinters of Geysir, Haukadalur, Iceland. *Sedimentology* **2007**, *54*, 921–948, doi:10.1111/j.1365-3091.2007.00866.x.

56. Lynne, B.Y.; Campbell, K.A.; James, B.J.; Browne, P.R.L.; Moore, J. Tracking crystallinity in siliceous hot-spring deposits. *Am. J. Sci.* **2007**, *307*, 612–641, doi:10.2475/03.2007.03.

57. Brocks, J.J.; Buick, R.; Logan, G.A.; Summons, R.E. Composition and syngeneity of molecular fossils from the 2.78 to 2.45 billion-year-old Mount Bruce Supergroup, Pilbara Craton, Western Australia. *Geochim. Cosmochim. Acta* **2003**, *67*, 4289–4319, doi:10.1016/s0016-7037(03)00208-4.

58. Brocks, J.J.; Buick, R.; Summons, R.E.; Logan, G.A. A reconstruction of Archean biological diversity based on molecular fossils from the 2.78 to 2.45 billion-year-old Mount Bruce Supergroup, Hamersley Basin, Western Australia. *Geochim. Cosmochim. Acta* **2003**, *67*, 4321–4335, doi:10.1016/s0016-7037(03)00209-6.

59. Jones, B.; Renaut, R.W.; Rosen, M.R. Biogenicity of Silica Precipitation around Geysers and Hot-Spring Vents, North Island, New Zealand. *J. Sediment. Res.* **1997**, *67*, 88–104, doi:10.1306/D42684FF-2B26-11D7-8648000102C1865D.

60. Jones, B.; Renaut, R.W.; Rosen, M.R. Stromatolites Forming in Acidic Hot-Spring Waters, North Island, New Zealand. *Palaios* **2000**, *15*, 450–475, doi:10.2307/3515515.

61. Jones, B.; Renaut, R.W.; Rosen, M.R. Silicified Microbes in a Geyser Mound: The Enigma of Low-Temperature Cyanobacteria in a High-Temperature Setting. *PALAIOS* **2003**, *18*, 87–109, doi:10.1669/0883-1351(2003)182.0.co;2.

62. Jones, B.; De Ronde, C.E.J.; Renaut, R.W.; Owen, R.B. Siliceous sublacustrine spring deposits around hydrothermal vents in Lake Taupo, New Zealand. *J. Geol. Soc.* **2007**, *164*, 227–242, doi:10.1144/0016-76492005-102.

63. Campbell, K.A.; Sannazzaro, K.; Rodgers, K.; Herdianita, N.; Browne, P. Sedimentary Facies and Mineralogy of the Late Pleistocene Umukuri Silica Sinter, Taupo Volcanic Zone, New Zealand. *J. Sediment. Res.* **2001**, *71*, 727–746, doi:10.1306/2dc40964-0e47-11d7-8643000102c1865d.

64. Hinman, N.W.; Walter, M.R. Textural Preservation in Siliceous Hot Spring Deposits During Early Diagenesis: Examples from Yellowstone National Park and Nevada, USA. *J. Sediment. Res.* **2005**, *75*, 200–215, doi:10.2110/jsr.2005.016.

65. Schinteie, R.; Campbell, K.A.; Browne, P.R.L. Microfacies of stromatolitic sinter from acid-sulphate-chloride springs at Parariki Stream, Rotokawa Geothermal Field, New Zealand. *Palaeontol. Electron.* **2007**, *10*, 33.

66. Campbell, K.A.; Lynne, B.Y.; Handley, K.M.; Jordan, S.; Farmer, J.D.; Guido, D.M.; Foucher, F.; Turner, S.; Perry, R.S. Tracing Biosignature Preservation of Geothermally Silicified Microbial Textures into the Geological Record. *Astrobiology* **2015**, *15*, 858–882, doi:10.1089/ast.2015.1307.

67. Wilmeth, D.T.; Corsetti, F.A.; Bisenic, N.; Dornbos, S.Q.; Oji, T.; Gonchigdorj, S. Punctuated Growth of Microbial Cones within Early Cambrian Oncoids, Bayan Gol Formation, Western Mongolia. *Palaios* **2015**, *30*, 836–845, doi:10.2110/palo.2015.014.

68. Hamilton, A.R.; Campbell, K.A.; Guido, D.M. Atlas of siliceous hot spring deposits (sinter) and other silicified surface manifestations in epithermal environments. *GNS Sci. Rep.* **2019**, 1–56, doi:10.21420/BQDR-XQ16.

69. Jones, B.; Renaut, R.W.; Konhauser, K.O. Genesis of large siliceous stromatolites at Frying Pan Lake, Waimangu geothermal field, North Island, New Zealand. *Sedimentology* **2005**, *52*, 1229–1252, doi:10.1111/j.1365-3091.2005.00739.x.

70. Gong, J.; Myers, K.D.; Munoz-Saez, C.; Homann, M.; Rouillard, J.; Wirth, R.; Schreiber, A.; Van Zuilen, M.A. Formation and Preservation of Microbial Palisade Fabric in Silica Deposits from El Tatio, Chile. *Astrobiology* **2020**, *20*, 500–524, doi:10.1089/ast.2019.2025.

71. Guidry, S.A.; Chafetz, H.S. Anatomy of siliceous hot springs: Examples from Yellowstone National Park, Wyoming, USA. *Sediment. Geol.* **2003**, *157*, 71–106, doi:10.1016/s0037-0738(02)00195-1.

72. Lynne, B.Y. Mapping vent to distal-apron hot spring paleo-flow pathways using siliceous sinter architecture. *Geothermics* **2012**, *43*, 3–24, doi:10.1016/j.geothermics.2012.01.004.

73. Ward, D.M.; Castenholz, R.W. Cyanobacteria in geothermal habitats. In *Ecology of Cyanobacteria: Their Diversity in Time and Space*; Whitton, B.A., Potts, M., Eds.; Kluwer: Dordrecht, The Netherlands, 2000; pp. 37–59.

74. Doemel, W.N.; Brock, T.D. The Physiological Ecology of Cyanidium caldarium. *J. Gen. Microbiol.* **1971**, *67*, 17–32, doi:10.1099/00221287-67-1-17.

75. Hoiczyk, E. Structural and Biochemical Analysis of the Sheath of Phormidium uncinatum. *J. Bacteriol.* **1998**, *180*, 3923–3932, doi:10.1128/jb.180.15.3923-3932.1998.

76. Jones, B.; Renaut, R.W.; Rosen, M.R. Vertical Zonation of Biota in Microstromatolites Associated with Hot Springs, North Island, New Zealand. *PALAIOS* **1997**, *12*, 220, doi:10.2307/3515424.

77. Huber, R.; Eder, W.; Heldwein, S.; Wanner, G.; Huber, H.; Rachel, R.; Stetter, K.O. Thermocrinis ruber gen. nov., sp. nov., a Pink-Filament-Forming Hyperthermophilic Bacterium Isolated from Yellowstone National Park. *Appl. Environ. Microbiol.* **1998**, *64*, 3576–3583, doi:10.1128/aem.64.10.3576-3583.1998.

78. Inoue, N.; Emi, T.; Yamane, Y.; Kashino, Y.; Koike, H.; Satoh, K. Effects of High-Temperature Treatments on a Thermophilic Cyanobacterium Synechococcus vulcanus. *Plant Cell Physiol.* **2000**, *41*, 515–522, doi:10.1093/pcp/41.4.515.

79. Ciniglia, C.; Yoon, H.S.; Pollio, A.; Pinto, G.; Bhattacharya, D. Hidden biodiversity of the extremophilic Cyanidiales red algae. *Mol. Ecol.* **2004**, *13*, 1827–1838, doi:10.1111/j.1365-294x.2004.02180.x.

80. LaLonde, S.V.; Konhauser, K.O.; Reysenbach, A.-L.; Ferris, F.G. The experimental silicification of Aquificales and their role in hot spring sinter formation. *Geobiology* **2005**, *3*, 41–52, doi:10.1111/j.1472-4669.2005.00042.x.

81. Inagaki, F.; Hayashi, S.; Doi, K.; Motomura, Y.; Izawa, E.; Ogata, S. Microbial participation in the formation of siliceous deposits from geothermal water and analysis of the extremely thermophilic bacterial community. *FEMS Microbiol. Ecol.* **1997**, *24*, 41–48, doi:10.1111/j.1574-6941.1997.tb00421.x.

82. Yoon, H.S.; Ciniglia, C.; Wu, M.; Comeron, J.M.; Pinto, G.; Pollio, A.; Bhattacharya, D. Establishment of endolithic populations of extremophilic Cyanidiales (Rhodophyta). *BMC Evol. Biol.* **2006**, *6*, 78, doi:10.1186/1471-2148-6-78.

83. Flores, G.E.; Liu, Y.; Ferrera, I.; Beveridge, T.J.; Reysenbach, A.-L. Sulfurihydrogenibium kristjanssonii sp. nov., a hydrogen- and sulfur-oxidizing thermophile isolated from a terrestrial Icelandic hot spring. *Int. J. Syst. Evol. Microbiol.* **2008**, *58*, 1153–1158, doi:10.1099/ijs.0.65570-0.

84. Reeb, V.; Bhattacharya, D. The Thermo-Acidophilic *Cyanidiophyceae* (Cyanidiales). In *Red Algae in the Genomic Age*; Springer International Publishing: Dordrecht, The Netherlands, 2010; Volume 13, pp. 409–426.

85. Hugo, R.C.; Cady, S.L.; Smythe, W. The Role of Extracellular Polymeric Substances in the Silicification of Calothrix: Evidence from Microbial Mat Communities in Hot Springs at Yellowstone National Park, USA. *Geomicrobiology* **2011**, *28*, 667–675, doi:10.1080/01490451.2010.511983.

86. Skorupa, D.; Reeb, V.; Castenholz, R.; Bhattacharya, D.; McDermott, T. Cyanidiales diversity in Yellowstone National Park. *Lett. Appl. Microbiol.* **2013**, *57*, 459–466, doi:10.1111/lam.12135.

87. Smythe, W.F.; McAllister, S.M.; Hager, K.W.; Hager, K.R.; Tebo, B.M.; Moyer, C.L. Silica Biomineralization of Calothrix-Dominated Biofacies from Queen's Laundry Hot-Spring, Yellowstone National Park, USA. *Front. Environ. Sci.* **2016**, *4*, 4, doi:10.3389/fenvs.2016.00040.

88. Phoenix, V.R.; Martinez, R.E.; Konhauser, K.O.; Ferris, F.G. Characterization and Implications of the Cell Surface Reactivity of Calothrix sp. Strain KC97. *Appl. Environ. Microbiol.* **2002**, *68*, 4827–4834, doi:10.1128/aem.68.10.4827-4834.2002.

89. Takacs, C.D.; Ehringer, M.; Favre, R.; Cermola, M.; Eggertsson, G.; Palsdottir, A.; Reysenbach, A.-L.; Favre, R. Phylogenetic characterization of the blue filamentous bacterial community from an Icelandic geothermal spring. *FEMS Microbiol. Ecol.* **2001**, *35*, 123–128, doi:10.1111/j.1574-6941.2001.tb00795.x.

90. Blank, C.E.; Cady, S.L.; Pace, N.R. Microbial Composition of Near-Boiling Silica-Depositing Thermal Springs throughout Yellowstone National Park. *Appl. Environ. Microbiol.* **2002**, *68*, 5123–5135, doi:10.1128/aem.68.10.5123-5135.2002.

91. Castenholz, R.W.; McDermott, T.R. The Cyanidiales: Ecology, Biodiversity, and Biogeography. In *Red Algae in the Genomic Age*; Springer International Publishing: Dordrecht, The Netherlands, 2010; Volume 13, pp. 357–371.

92. Konhauser, K.O. Bacterial iron biomineralisation in nature. *FEMS Microbiol. Rev.* **1997**, *20*, 315–326, doi:10.1111/j.1574-6976.1997.tb00317.x.

93. Konhauser, K.O. Diversity of bacterial iron mineralization. *Earth-Science Rev.* **1998**, *43*, 91–121, doi:10.1016/s0012-8252(97)00036-6.

94. Phoenix, V.R.; Konhauser, K.O.; Ferris, F.G. Experimental study of iron and silica immobilization by bacteria in mixed Fe-Si systems: Implications for microbial silicification in hot springs. *Can. J. Earth Sci.* **2003**, *40*, 1669–1678, doi:10.1139/e03-044.

95. Jones, B.; Renaut, R.W. Selective mineralization of microbes in Fe-rich precipitates (jarosite, hydrous ferric oxides) from acid hot springs in the Waiotapu geothermal area, North Island, New Zealand. *Sediment. Geol.* **2007**, *194*, 77–98, doi:10.1016/j.sedgeo.2006.05.025.

96. Vollrath, S.; Behrends, T.; Van Cappellen, P. Oxygen Dependency of Neutrophilic Fe(II) Oxidation by Leptothrix Differs from Abiotic Reaction. *Geomicrobiol. J.* **2012**, *29*, 550–560, doi:10.1080/01490451.2011.594147.

97. Fleming, E.J.; Cetinić, I.; Chan, C.S.; King, D.W.; Emerson, D. Ecological succession among iron-oxidizing bacteria. *ISME J.* **2013**, *8*, 804–815, doi:10.1038/ismej.2013.197.

98. Rodgers, K.; Browne, P.; Buddle, T.; Cook, K.; Greatrex, R.; Hampton, W.; Herdianita, N.; Holland, G.; Lynne, B.; Martin, R.; et al. Silica phases in sinters and residues from geothermal fields of New Zealand. *Earth Sci. Rev.* **2004**, *66*, 1–61, doi:10.1016/j.earscirev.2003.10.001.

99. Cady, S.L.; Farmer, J.D. Fossilization Processes in Siliceous Thermal Springs: Trends in Preservation Along Thermal Gradients. *Novartis Foundation Symposia* **2007**, *202*, 150–173, doi:10.1002/9780470514986.ch9.

100. Setiawan, F.A.; Rahayuningsih, E.; Petrus, H.T.B.M.; Nurpratama, M.I.; Perdana, I. Kinetics of silica precipitation in geothermal brine with seeds addition: Minimizing silica scaling in a cold re-injection system. *Geotherm. Energy* **2019**, *7*, 1–16, doi:10.1186/s40517-019-0138-3.

101. Jones, B.; Konhauser, K.; Renaut, R.; Wheeler, R. Erratum to Microbial silicification in Iodine Pool, Waimangu geothermal area, North Island, New Zealand: Implications for recognition and identification of ancient silicified microbes. *J. Geol. Soc.* **2005**, *162*, 576.2–576, doi:10.1144/0016-7649er161-6a.

102. Pancost, R.D.; Pressley, S.; Coleman, J.M.; Talbot, H.M.; Kelly, S.P.; Farrimond, P.; Schouten, S.; Benning, L.; Mountain, B.W. Composition and implications of diverse lipids in New Zealand Geothermal sinters. *Geobiology* **2006**, *4*, 71–92, doi:10.1111/j.1472-4669.2006.00069.x.

103. Hetzer, A.; Morgan, H.W.; McDonald, I.R.; Daughney, C.J. Microbial life in Champagne Pool, a geothermal spring in Waiotapu, New Zealand. *Extremophiles* **2007**, *11*, 605–614, doi:10.1007/s00792-007-0073-2.

104. Kaur, G.; Mountain, B.W.; Hopmans, E.C.; Pancost, R.D. Relationship between lipid distribution and geochemical environment within Champagne Pool, Waiotapu, New Zealand. *Org. Geochem.* **2011**, *42*, 1203–1215, doi:10.1016/j.orggeochem.2011.08.006.

105. Huber, R.; Wilharm, T.; Huber, D.; Trincone, A.; Burggraf, S.; König, H.; Reinhard, R.; Rockinger, I.; Fricke, H.; Stetter, K.O. Aquifex pyrophilus gen. nov. sp. nov., Represents a Novel Group of Marine Hyperthermophilic Hydrogen-Oxidizing Bacteria. *Syst. Appl. Microbiol.* **1992**, *15*, 340–351, doi:10.1016/s0723-2020(11)80206-7.

106. Huber, R.; Rossnagel, P.; Woese, C.; Rachel, R.; Langworthy, T.; Stetter, K. Formation of Ammonium from Nitrate During Chemolithoautotrophic Growth of the Extremely Thermophilic Bacterium Ammonifex degensii gen. nov. sp. nov. *Syst. Appl. Microbiol.* **1996**, *19*, 40–49, doi:10.1016/s0723-2020(96)80007-5.

107. Langworthy, T.A.; Holzer, G.; Zeikus, J.G.; Tornabene, T.G. Iso- and Anteiso-Branched Glycerol Diethers of the Thermophilic Anaerobe Thermodesulfotobacterium commune. *Syst. Appl. Microbiol.* **1983**, *4*, 1–17, doi:10.1016/s0723-2020(83)80029-0.

108. Knudsen, E.; Jantzen, E.; Bryn, K.; Ormerod, J.G. Quantitative and structural characteristics of lipids in Chlorobium and Chloroflexus. *Arch. Microbiol.* **1982**, *132*, 149–154, doi:10.1007/bf00508721.

109. Zelles, L. Identification of single cultured micro-organisms based on their whole-community fatty acid profiles, using an extended extraction procedure. *Chemosphere* **1999**, *39*, 665–682, doi:10.1016/s0045-6535(99)00131-9.

110. Jahnke, L.L.; Embaye, T.; Hope, J.; Turk, K.A.; Van Zuilen, M.; Marais, D.J.D.; Farmer, J.D.; Summons, R.E. Lipid biomarker and carbon isotopic signatures for stromatolite-forming, microbial mat communities and Phormidium cultures from Yellowstone National Park. *Geobiology* **2004**, *2*, 31–47, doi:10.1111/j.1472-4677.2004.00021.x.

111. Zelles, L. Phospholipid fatty acid profiles in selected members of soil microbial communities. *Chemosphere* **1997**, *35*, 275–294, doi:10.1016/s0045-6535(97)00155-0.

112. Grimalt, J.O.; De Wit, R.; Teixidor, P.; Albaigés, J. Lipid biogeochemistry of Phormidium and Microcoleus mats. *Org. Geochem.* **1992**, *19*, 509–530, doi:10.1016/0146-6380(92)90015-p.

113. Zeng, Y.; Ward, D.M.; Brassell, S.C.; Eglinton, G. Biogeochemistry of hot spring environments. 2, Lipid compositions of Yellowstone (Wyoming, USA) cyanobacterial and *Chloroflexus* mats. *Chem. Geol.* **1992**, *95*, 327–345, doi:10.1016/0009-2541(92)90020-6.

114. Zeng, Y.; Ward, D.M.; Brassell, S.C.; Eglinton, G. Biogeochemistry of hot spring environments. 3, Apolar and polar lipids in the biologically-active layers of a cyanobacterial mat. *Chem. Geol.* **1992**, *95*, 347–360, doi:10.1016/0009-2541(92)90021-v.

115. Talbot, H.M.; Farrimond, P.; Schaeffer, P.; Pancost, R.D. Bacteriohopanepolyols in hydrothermal vent biogenic silicates. *Org. Geochem.* **2005**, *36*, 663–672, doi:10.1016/j.orggeochem.2004.10.015.

116. Shiea, J.; Brassel, S.C.; Ward, D.M. Comparative analysis of extractable lipids in hot spring microbial mats and their component photosynthetic bacteria. *Org. Geochem.* **1991**, *17*, 309–319, doi:10.1016/0146-6380(91)90094-z.

117. Matsumoto, G.I.; Ohtani, S.; Hirota, K. Biogeochemical feature of hydrocarbons on cyanobacterial mats from the McMurdo Dry Valleys, Antarctica. Proceedings of the National Institute of Polar Research (NIPR). *Symp. Polar Biol.* **1993**, *6*, 98–105.

118. Wada, H.; Murata, N. Membrane Lipids in Cyanobacteria. In *Lipids in Photosynthesis: Structure, Function and Genetics*; Springer International Publishing: Dordrecht, The Netherlands, 2006; Volume 6, pp. 65–81.

119. Teece, B.L.; George, S.C.; Djokic, T.; Campbell, K.A.; Ruff, S.W.; Van Kranendonk, M.J. Biomolecules from Fossilized Hot Spring Sinters: Implications for the Search for Life on Mars. *Astrobiology* **2020**, *20*, 537–551, doi:10.1089/ast.2018.2018.

120. Havig, J.R.; Raymond, J.; Meyer-Dombard, D.R.; Zolotova, N.; Shock, E.L. Merging isotopes and community genomics in a siliceous sinter-depositing hot spring. *J. Geophys. Res. Space Phys.* **2011**, *116*, doi:10.1029/2010jg001415.

121. Van Der Meer, M.T.J.; Schouten, S.; De Leeuw, J.W.; Ward, D.M. Autotrophy of green non-sulphur bacteria in hot spring microbial mats: Biological explanations for isotopically heavy organic carbon in the geological record. *Environ. Microbiol.* **2000**, *2*, 428–435, doi:10.1046/j.1462-2920.2000.00124.x.

122. Kjartansdóttir, R. Carbon Isotopes and Systematics of Icelandic Low-Temperature Geothermal Waters. Master's Thesis, University of Iceland, Reykjavik, Iceland, 3 October 2014; 39p.

123. Sveinbjörnsdóttir, A.E.; Arnórsson, S.; Heinemeier, J.; Ármannsson, H.; Kristmannsdóttir, H. Dissolved inorganic carbon isotopes in natural waters in Iceland. In *Water-Rock Interaction XIII*; Torres-Alvarado, P.A., Ed.; CRC Press: London, UK, 2010; pp. 99–102.

124. Sveinbjörnsdóttir, A.E.; Heinemeier, J.; Arnórsson, S. Isotopic characteristics (δ18O, δD, δ13C, 14C) of thermal waters in the Mosfellssveit and Reykjavík low-temperature areas, Iceland. In the Proceedings of the World Geothermal Congress, Antalya, Turkey, 24–29 April 2005; pp. 1–5.

125. Skirnisdottir, S.; Hreggvidsson, G.O.; Hjörleifsdottir, S.; Marteinsson, V.T.; Petursdottir, S.K.; Holst, O.; Kristjansson, J.K. Influence of Sulfide and Temperature on Species Composition and Community Structure of Hot Spring Microbial Mats. *Appl. Environ. Microbiol.* **2000**, *66*, 2835–2841, doi:10.1128/aem.66.7.2835-2841.2000.

126. Fernandez-Turiel, J.; Garcia-Valles, M.; Gimeno-Torrente, D.; Saavedra-Alonso, J.; Martinez-Manent, S. The hot spring and geyser sinters of El Tatio, Northern Chile. *Sediment. Geol.* **2005**, *180*, 125–147, doi:10.1016/j.sedgeo.2005.07.005.

127. Farmer, J.D.; Marais, D.J.D. Exploring for a record of ancient Martian life. *J. Geophys. Res. Space Phys.* **1999**, *104*, 26977–26995, doi:10.1029/1998je000540.

128. Ruff, S.W.; Campbell, K.A.; Van Kranendonk, M.J.; Rice, M.S.; Farmer, J.D. The Case for Ancient Hot Springs in Gusev Crater, Mars. *Astrobiology* **2020**, *20*, 475–499, doi:10.1089/ast.2019.2044.

129. Frydenvang, J.; Gasda, P.J.; Hurowitz, J.A.; Grotzinger, J.P.; Wiens, R.C.; Newsom, H.E.; Edgett, K.S.; Watkins, J.; Bridges, J.C.; Maurice, S.; et al. Diagenetic silica enrichment and late-stage groundwater activity in Gale crater, Mars. *Geophys. Res. Lett.* **2017**, *44*, 4716–4724, doi:10.1002/2017gl073323.